GEOSPHERE

GEOSPHERE, v. 17, no. 2

https://doi.org/10.1130/GES02275.1

20 figures; 2 tables

CORRESPONDENCE: akrabbenhoeft@geomar.de

CITATION: Krabbenhoeft, A., von Huene, R., Miller, J.J., and Klaeschen, D., 2021, Subducting oceanic basement roughness impacts on upper-plate tectonic structure and a backstop splay fault zone activated in the southern Kodiak aftershock region of the Mw 9.2, 1964 megathrust rupture, Alaska: Geosphere, v. 17, no. 2, p. 409–437, https://doi.org/10.1130/GES02275.1.

Science Editor: Shanaka de Silva
Guest Associate Editor: Laura M. Wallace

Received 16 April 2020
Revision received 26 October 2020
Accepted 5 January 2021

Published online 25 February 2021

Subducting oceanic basement roughness impacts on upper-plate tectonic structure and a backstop splay fault zone activated in the southern Kodiak aftershock region of the Mw 9.2, 1964 megathrust rupture, Alaska

Anne Krabbenhoeft[1,*], Roland von Huene[2,*], John J. Miller[3,*], and Dirk Klaeschen[1]

[1]GEOMAR Helmholtz Center for Ocean Research Kiel, Wischhofstr. 1-3, 24148 Kiel, Germany
[2]U.S. Geological Survey, Scientist Emeritus, Moffett Field, California 94035, USA
[3]U.S. Geological Survey, Scientist Emeritus, Denver Federal Center, Denver, Colorado 80225, USA

ABSTRACT

In 1964, the Alaska margin ruptured in a giant Mw 9.2 megathrust earthquake, the second largest during worldwide instrumental recording. The coseismic slip and aftershock region offshore Kodiak Island was surveyed in 1977–1981 to understand the region's tectonics. We re-processed multichannel seismic (MCS) field data using current standard Kirchhoff depth migration and/or MCS traveltime tomography. Additional surveys in 1994 added P-wave velocity structure from wide-angle seismic lines and multibeam bathymetry. Published regional gravity, backscatter, and earthquake compilations also became available at this time.

Beneath the trench, rough oceanic crust is covered by ~3–5-km-thick sediment. Sediment on the subducting plate modulates the plate interface relief. The imbricate thrust faults of the accreted prism have a complex P-wave velocity structure. Landward, an accelerated increase in P-wave velocities is marked by a backstop splay fault zone (BSFZ) that marks a transition from the prism to the higher rigidity rock beneath the middle and upper slope. Structures associated with this feature may indicate fluid flow. Farther upslope, another fault extends >100 km along strike across the middle slope. Erosion from subducting seamounts leaves embayments in the frontal prism.

Plate interface roughness varies along the subduction zone. Beneath the lower and middle slope, 2.5D plate interface images show modest relief, whereas the oceanic basement image is rougher. The 1964 earthquake slip maximum coincides with the leading and/or landward flank of a subducting seamount and the BSFZ. The BSFZ is a potentially active structure and should be considered in tsunami hazard assessments.

*E-mail: akrabbenoeft@geomar.de; rhuene@mindspring.com; jmiller@usgs.gov

INTRODUCTION

In subduction zones, evaluating the effects of rough subducting seafloor topography on subduction megathrust earthquakes is important for assessing seismic and tsunami hazards (Wang and Bilek, 2014; Lallemand et al., 2018, and references therein). Typically, rough subducting plate topography affects interplate boundary processes (e.g., Rosenbaum and Mo, 2011), and it may act as a barrier between earthquake aftershock regions (e.g., Nakai, Peru, Kodaira et al., 2000; Robinson et al., 2006). Scholz and Small (1997) propose that rough subducting oceanic plate topography could increase normal stress and seismic coupling along the plate interface and may therefore lead to large-magnitude earthquakes along the subducting megathrust. In contrast, Wang and Bilek (2011) propose that great earthquakes occur where the subducting megathrust plate interface is smooth, whereas upper-plate fracturing and aseismic creep may be favored where rough oceanic basement subducts. This would inhibit the generation of great megathrust earthquakes or result in multiple patches of slip and complex ruptures. Subducting plate topography also induces along-strike variation in trench and forearc morphology (e.g., Kopp, 2013).

Hydrologic systems and tectonic processes in subduction zones are tightly interconnected (Saffer and Tobin, 2011), including the generation of extensive thrust zones (Hubbert and Rubey, 1959), the control of wedge geometry (Davis et al., 1983), and the alteration of physical properties in sediments (Karig, 1990), thereby affecting deformation mechanics. The presence of fluids entrained during underthrusting of sediment and basement relief into the subduction zones leads to elevated pore fluid pressures with landward increasing load of the accretionary prism on the plate interface (von Huene et al., 2009). This may influence frictional properties and seismic slip behavior on the shallow subduction zone (Hubbert and Rubey, 1959; Byrne et al., 1988; Lallemand et al., 1994; Bangs et al., 2009).

Splay faults branching upward from the plate interface exist at many subduction boundaries and may play an important role in tsunami hazard (Moore et al., 2007). The activation of splay faults during megathrust ruptures can amplify coseismic vertical seafloor displacement (Moore et al., 2007), thus producing large tsunamis that are hazardous to neighboring coastal regions (Lay and Bilek, 2007; Wendt et al., 2009; Bilek, 2010). In several subduction settings, splay faults have been mapped with

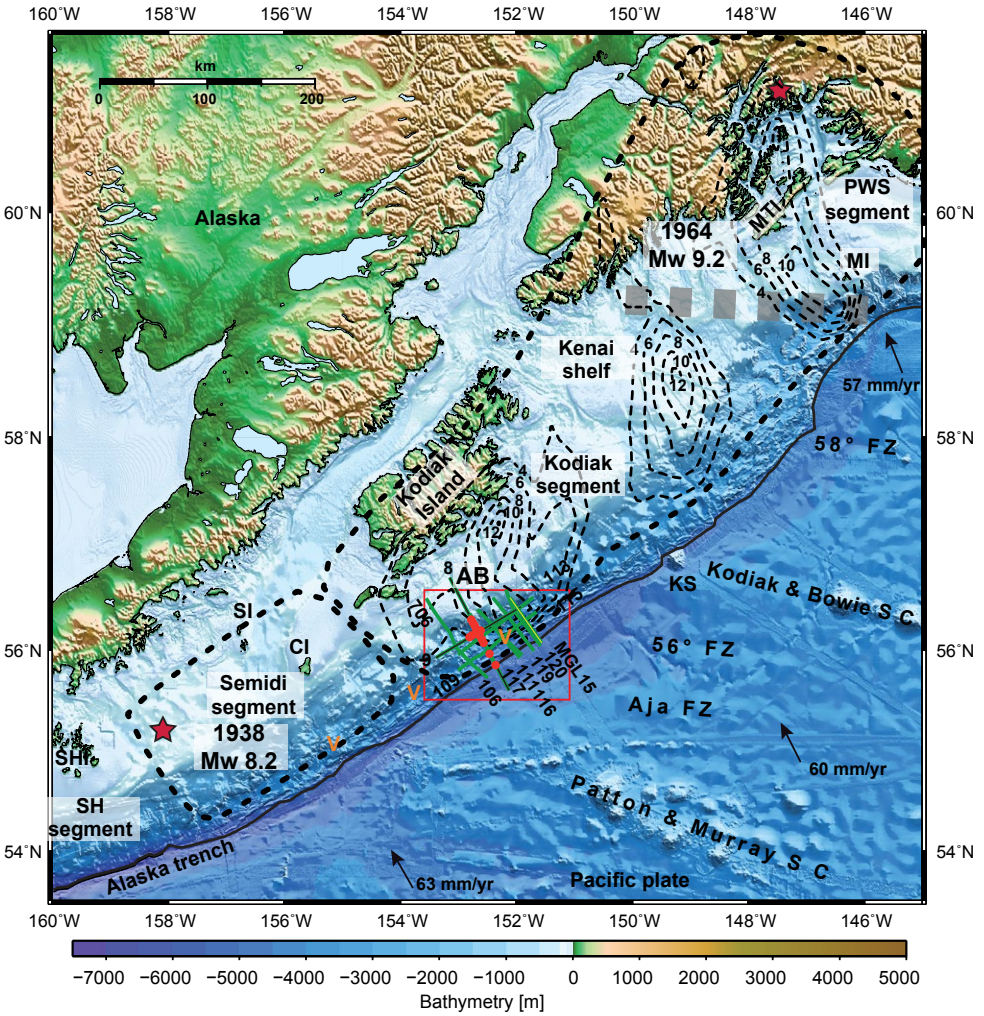

Figure 1. Bathymetric overview map of the Alaska subduction zone. Red stars denote epicenters of the 1964 giant and 1938 great Alaska subduction earthquakes; annotated Mw indicates earthquake moment magnitudes; and bold, black dashed lines encircle their afterslip regions. Black dashed annotated isolines in the 1964 giant earthquake region mark zones of the largest slip (m; after Ichinose et al., 2007). Rupture segments are annotated, and wide dashed gray line marks division of Prince William Sound and Kodiak segments. The solid black line marks the plate boundary. Annotated arrows show plate motion and velocity relative to the North American plate (MORVEL, DeMets et al., 2010). Numbered solid lines show seismic lines; green and light green—Albatross legacy and new multichannel seismic (MCS) data; black—wide-angle; red dots are ocean bottom hydrophone (OBH) locations. Figure A1 shows seismic profile and station locations in greater detail. PWS—Prince William Sound; MTI—Montague Island; MI—Middleton Island; FZ—fracture zone; KS—Kodiak Seamount; SC—Seamount chain; AB—Albatross Bank; CI—Chirikof Island; SI—Semidi Islands; SH—Shumagin; SHI—Shumagin Islands, orange V—vent locations. Red box marks region shown in Figures 9, 13, A1, and A6.

seismic methods, and in some subduction zones, they are proposed to be related to tsunami earthquakes; these include Japan 1896 (Kanamori, 1972), Nicaragua 1992 (Kanamori and Kikuchi, 1993), Unimak Alaska 1946 (Johnson and Satake, 1997; von Huene et al., 2016), and Java 2006 (Fan et al., 2017). In this study, we identify a splay fault zone at the transition of the lower slope accretionary prism to the middle continental slope at the backstop. We term such a splay fault zone as the "backstop splay fault zone" (BSFZ).

The forearc structure and seismic compressional velocities (Vp) are a measure of elastic properties. They document the patterns of permanent deformation that a margin has experienced over many seismic cycles (Sallarès and Ranero, 2019). In the southern Kodiak aftershock region following the giant Mw 9.2 1964 earthquake, we investigate the tectonic framework with multibeam bathymetry, multichannel and wide-angle seismic data, seismicity, and global gravity data to better understand the interaction of subducting plate topography with the trench and forearc structure. We find that even though rough subducting oceanic basement topography plays a modest role in affecting the BSFZ structure, structural features of the incoming igneous basement such as fracture zones affect upper-plate deformation in the accretionary prism to the middle slope. This occurs despite a ~1.5-km-thick, lower-plate sediment layer that moderates the impact of basement relief. Additionally, subducting oceanic basement relief may play a major role in redirecting megathrust slip up the BSFZ rather than beneath the outer accretionary prism.

Tectonic Setting

The Mw 9.2 earthquake of 28 March 1964 was the largest instrumentally documented earthquake in Alaska and the second largest in the instrumental record (Christensen and Beck, 1994). It ruptured 680–740 km of convergent plate boundary between the Pacific and North American plates from Middleton Island in the northeast to Albatross Bank in the southwest (Fig. 1, Plafker, 1965; Johnson et al., 1996; Ichinose et al., 2007). Two areas of the highest

coseismic moment release correspond with two aftershock regions named the Prince William Sound and Kodiak aftershock regions (Fig. 1). The Prince William Sound aftershock region is the site of collision of the Yakutat terrane with North America (e.g., Lahr et al., 1988; Gulick et al., 2007). The Kodiak aftershock region is a typical convergent margin subduction zone and has been active since Cretaceous time. In the downdip direction, the Kodiak rupture zone is ~150 km wide (e.g., Savage et al., 1999; Sauber et al., 2006). In the Kodiak region, two areas of large slip occurred beneath the continental shelf and slope. The northeastern portion of the Kodiak rupture segment occurred seaward of the Kenai shelf, and the other is in the southwest, offshore Kodiak Island (Fig. 1). The northeastern rupture segment is located on the 58° subducting fracture zone associated with many seamounts that are buried by Surveyor fan and Alaska trench sediment (von Huene et al., 2012, Fig. 1). The southwestern area of large slip is subdivided into two centers of 12-m slip (Ichinose et al., 2007). One lies on the projection of the subducted Kodiak and Bowie Seamount chain that is marked by Kodiak Seamount in the Alaska trench axis (Fig. 1). The other slip center extends seaward of Albatross Bank to the trench axis and lies at the continuation of an E-W–oriented subducting fracture zone system (Fig. 1), including the 56° fracture zone (Naugler and Wageman, 1973; Reece et al., 2013). On the outer rise, that fracture zone system ruptured during the unusual 23 January 2018 intra-oceanic plate Mw 7.9 Gulf of Alaska strike-slip earthquake, an aftershock region of the giant 1964 earthquake (Krabbenhoeft et al., 2018; Lay et al., 2018; Ruppert et al., 2018).

The average velocity of plate convergence is ~60 mm/yr (DeMets et al., 2010) and almost normal to the trench in the Kodiak aftershock region (shown by arrows, Fig. 1). However, N-S–aligned oceanic crustal fabric trends ~30° oblique to the trench (Krabbenhoeft et al., 2018) and parallel to ocean plate-bending faults, expressed in regional multibeam bathymetry (Reece et al., 2013). Paleoseismic studies of uplift rates in silt-peat sequences of the Copper River Delta (Reimnitz, 1966; Plafker et al., 1992) and reconstructions of coseismic uplift of marine terraces on Middleton Island indicate recurrence intervals of megathrust earthquakes similar to the 1964 event ranging from ~400 to ~1400 years (Plafker, 1987; Goes, 1996; Carver and Plafker, 2008; and references therein). Smaller megathrust earthquakes (magnitudes ranging from 7.5 to 9.2) in the Kodiak aftershock region occurred more frequently, on the order of 4–64 years (Goes, 1996, and references therein).

To the southwest, the landward extension of the Patton and Murray Seamount chain separates the Kodiak aftershock region from the Semidi aftershock region that ruptured in the 1938 Mw 8.2 earthquake (Fig. 1). However, no structural link between the subducted Patton and Murray Seamount chain and the rupture boundary has been reported so far despite their common location. Farther southwest of the Kodiak aftershock region, BSFZs have been identified in the Alaskan subduction zone segments as far as the Unimak segment, where they form the transition between the lower slope and the backstop at the base of the middle slope. Variations of the BSFZ along the Alaska-Aleutian subduction zone are discussed by von Huene et al. (2020). The BSFZ has been identified as a continuous structure along the entire length of the Semidi region (Fig. 1, von Huene et al., 2015) into the Unimak region (von Huene et al., 2016, 2019). All Alaska margin regions have ruptured in great earthquakes during the time of instrumental recording except the Shumagin area. The Semidi margin rupture in the 1938 Mw 8.2 earthquake produced only a small tsunami because of the great depth of the rupture. The BSFZ has possibly played a role in past great earthquakes and tsunamis in this part of Alaska, although this is difficult to determine definitively with existing data. A splay fault seaward of the mid-slope terrace has been proposed as possibly involved in the far-field tsunami source of the 1946 Unimak tsunami earthquake (von Huene et al., 2016).

Alaskan megathrust earthquakes have been very destructive in the past, and a future earthquake may cause significant damage from local as well as trans-oceanic tsunamis. This paper is a contribution to understanding structures and processes that may be involved in Alaskan megathrust ruptures. Our study involves a combination of seafloor morphology with a network of reprocessed seismic data to show the distribution of splay faults in the margin wedge as well as subducting oceanic basement relief and its impact on upper-plate tectonic structures. Our study is focused seaward of Albatross Bank in the 1964 southern Kodiak aftershock region, which hosted the largest coseismic slip (Ichinose et al., 2007, Fig. 1) during 1964 and an afterslip maximum (Suito and Freymueller, 2009).

GEOPHYSICAL DATA AND METHODS

Bathymetric Data

Regional multibeam bathymetric data (Flueh and von Huene, 1994; Suess, 1994; Reece et al., 2013; Shillington et al., 2015) were processed using the MB-System (Caress and Chayes, 1996, 2017; Caress et al., 2008) and GMT (Wessel and Smith, 1998), both open-source processing software packages. The bathymetry grids, 150 m × 150 m for the overview map and 100 m × 100 m for the detailed maps (e.g., Fig. A1), were calculated using the WGS84 horizontal datum and a Gaussian weighted mean filter gridding algorithm (Caress and Chayes, 1996, 2017; Caress et al., 2008). In regions with no ship-depth soundings, a compilation of Lim et al. (2009), the GEBCO 30 arc-second global grid of elevations, the GEBCO_2014 Grid (Becker et al., 2009; Weatherall et al., 2015), and the GEBCO 2019 grid (GEBCO Compilation Group, 2019) were combined with the processed multibeam bathymetry grid to create the bathymetric maps (Fig. 1).

Seismic Data

In this study, wide-angle data acquired in 1994 from ocean bottom hydrophones (OBHs; Flueh and Bialas, 1996; Figs. 2–4) and coincident multichannel seismic (MCS) data were used to obtain the structural images and P-wave velocity-depth models of the subduction zone in the Albatross and adjacent regions of the Alaskan subduction zone. MCS legacy data acquired by the U.S. Geological Survey (USGS) research vessel (RV) *S.P. Lee* in 1977 and 1981 (cruises L-7-77-WG and L-7-81-WG, available at https://walrus.wr.usgs.gov/namss/; Bruns et al.,

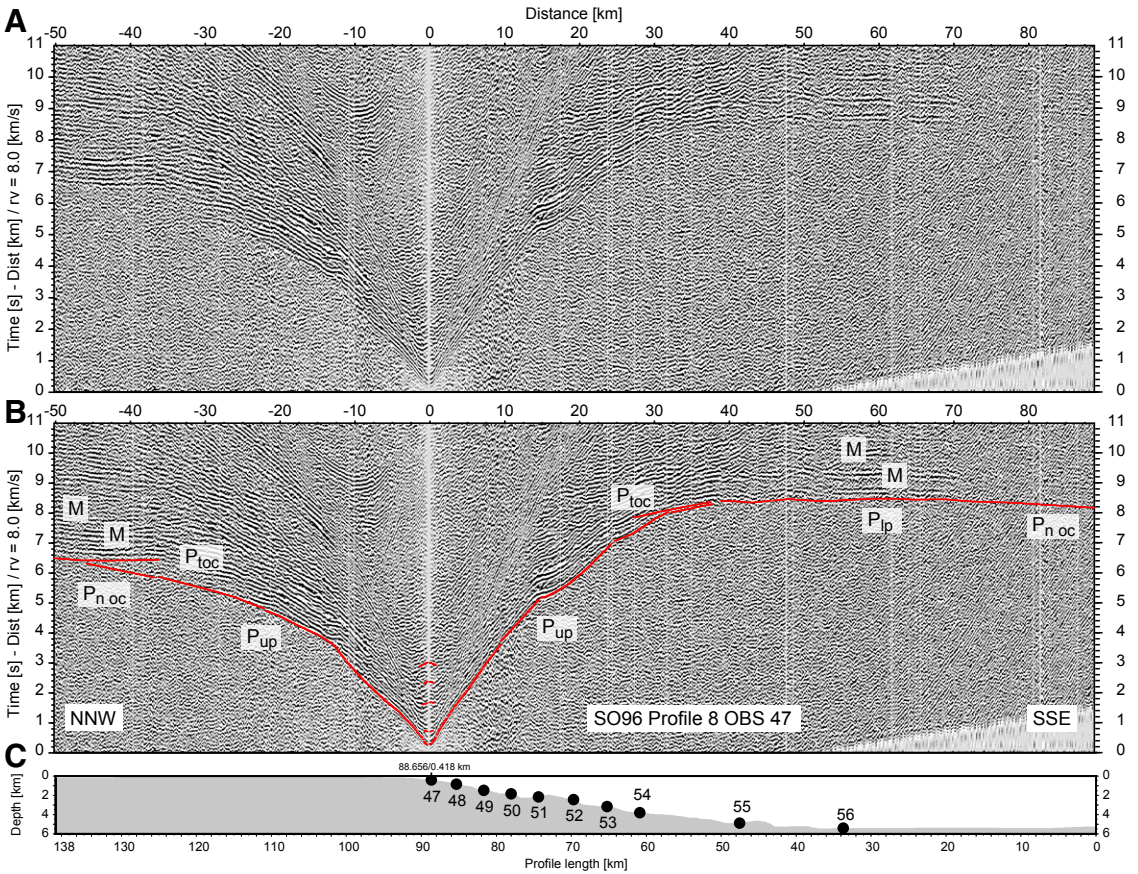

Figure 2. (A) Ocean bottom hydrophone (OBH) data example at landward end of profile P8 displayed with reduced velocity (rv) of 8 km/s. (B) Calculated traveltimes (red) through final velocity depth model with OBH section. Picked phases (red) include: P_{up}—refraction through upper plate; P_{lp}—refraction through lower plate; P_{pi}—reflection of plate interface; P_{uc}—reflection of upper crust; P_{toc}—reflection of top of oceanic crust of subducting plate; P_mP_{oc}—reflection of oceanic Moho; P_{noc}—refraction through subducting oceanic mantle; M—multiple. (C) Depth section of profile P8 with OBH stations indicated by numbered filled circles.

1987) as well as one recently acquired MCS line with RV *M.G. Langseth* (line MGL15 of cruise L-09-11-GA; Frederik, 2016, available at https://walrus.wr.usgs.gov/namss/) were investigated.

The OBH and MCS data were processed using an iterative process. The depth-converted P-wave velocity model for the preliminary pre-stack time migration (MGL15) served as a reference starting model for the OBH seismic 2D joint refraction and reflection tomography (Korenaga et al., 2000). The final P-wave velocity models are shown in Figures 5, A2, and A3. The result of the 2D refraction and reflection tomography was the starting model for the Kirchhoff pre-stack depth migration (PSDM) of the MCS data. MCS lines MGL15 (Fig. 6) and 117 (Fig. 7) were studied in greater detail, and therefore the velocity-depth models were derived in a more time-consuming way by using the data-driven traveltime reflection tomography.

Reprocessing MCS data improved and constrained the image of the upper, sedimentary structure of the margin. OBH seismic tomography processing was aimed at constraining the P-wave velocity model, in particular for the deeper part of the margin (e.g., the crustal structure) as well as the geometry of the subduction plate interface to the oceanic crust Moho. A detailed description of the seismic methods is given in the Appendix.

RESULTS

We start with the seaward part and successively proceed landward up to the shelf of the 1964 southern Kodiak aftershock region. Note that some morphological structures become more clear when viewed with the background of subsurface structures in seismic images of the following section.

Bathymetric Studies—Seafloor Morphology

The seafloor of the incoming Pacific plate is smooth, except for a few seamounts and ridges.

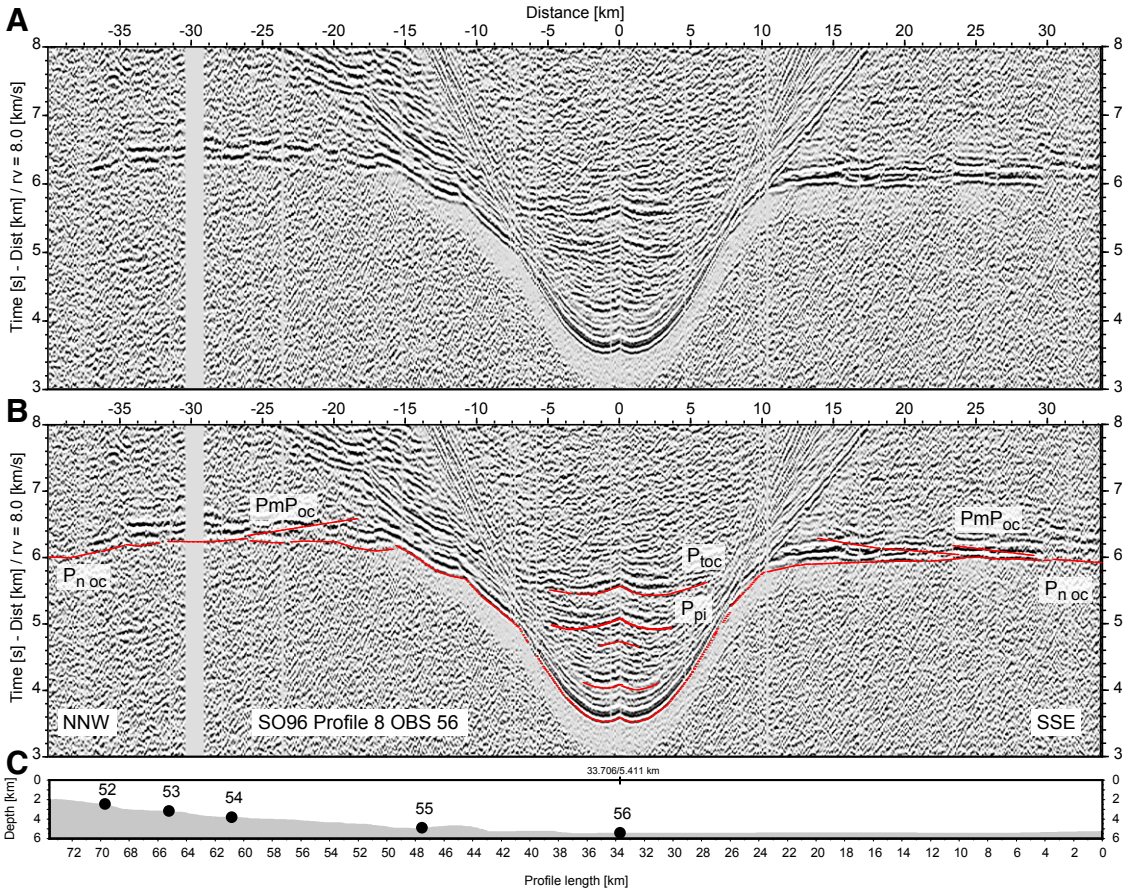

Figure 3. (A) Ocean bottom hydrophone (OBH) data example at seaward end of profile P8 displayed with reduced velocity (rv) of 8 km/s. (B) Calculated traveltimes (red) through final velocity depth model with OBH section. Picked phases (red) include: P_{pi} —reflection of plate interface; P_{toc}—reflection of top of oceanic crust of subducting plate; P_mP_{oc}—reflection of oceanic Moho; P_{noc}—refraction through subducting oceanic mantle. (C) Depth section of profile P8 with OBH stations indicated by numbered filled circles.

Long-wavelength structures conform to underlying fracture zone systems (Figs. 1, 8, and A4). Subtle plate-bending faults parallel to seafloor spreading fabric and at 30° to the trench axis (Fig. 9) are only visible with high-resolution multibeam bathymetry (e.g., Reece et al., 2013; Krabbenhoeft et al., 2018). The ~5.5-km-deep trench has a smooth seafloor.

Across the forearc, two major contrasting morphology domains are evident in the perspective diagram of the original multibeam bathymetry (Fig. 9): a shallow-dipping, smooth lower slope and a steep and rough middle and upper slope (Fig. A5). The lower slope shows long trench-parallel ridges in a zone adjacent to the trench axis (Fig. 9). Three embayments or "cookie bites" incise the accretionary ridges of the margin toe (Fig. 9), which are commonly associated with subducting seamounts or ridges that erode the prism. The transition between the two differing tectonic domains from lower to middle slope is broadly defined in the morphology. Its seafloor expression is marked by the BSFZ (Fig. 9), an along-strike continuous structure of major splay faults that displace the seafloor up to ~200 m (e.g., Fig. 6). The BSFZ forms a ridge at the slope break between accretionary and middle prism (Fig. 9). The steep middle to upper slope owes its morphology to competent older rock such as that of Eocene age. Rock of Eocene age was drilled on the shelf edge (Turner et al., 1987) and imaged seismically a short distance down the upper slope (Winston, 1983). The lower-slope ridges paralleling the trench axis indicate the accretionary prism (Miller and von Huene, 1987; von Huene et al., 2012). The cross-sectional area of the accretionary prism is roughly equivalent to the sediment volume that would be accreted to the prism in <1 m.y., assuming present convergence rates and trench sediment thickness (von Huene et al., 1998). Therefore, the difference in age between Eocene rock of the steep

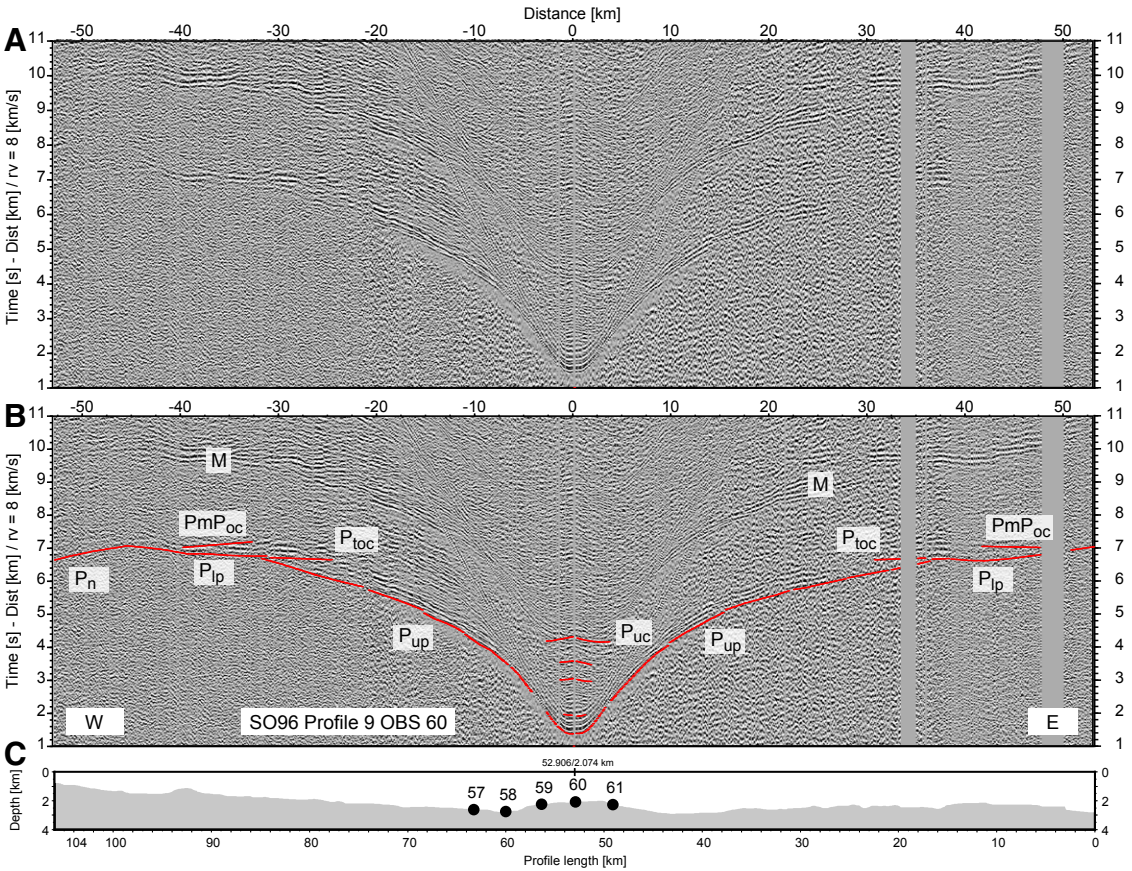

Figure 4. (A) Ocean bottom hydrophone (OBH) data example of profile P9 displayed with reduced velocity (rv) of 8 km/s. (B) Calculated traveltimes (red) through final velocity depth model with OBH section. Picked phases (red) include: P_{pi}—reflection of plate interface; P_{toc}—reflection of top of oceanic crust of subducting plate; P_mP_{oc}—reflection of oceanic Moho; P_n—refraction through subducting oceanic mantle; M—multiple. (C) Depth section of profile P9 with OBH stations indicated by numbered filled circles.

slope and accreted trench sediment is unquestionably large (ca. 30–50 Ma).

The current seafloor morphology appears to have been shaped by relief that subducted during the Quaternary. A broad age reference is the glacial channel extending across the shelf from Kodiak Island that empties onto the slope to form a canyon where line 111 is located (Figs. 1, 9, A1, and A4). The channel terminates at the accretionary prism, indicating the prism postdates glaciation. Southwest of line 117, multibeam bathymetry across the middle slope (Figs. 9 and A1) shows transverse lineaments paralleling the plate convergence vector or roughly ~85° to the trench axis and regional trend. These plate vector-parallel lineaments may suggest subduction of significant lower-plate relief that also predates the current accretionary prism. Additionally, the seafloor morphology of this area shows rough small-scale (~100–200-m-high and ~100-m- to 3–4-km-across) blocks or small cones (Fig. A1, between seismic lines 106, 117, 113, and 109). A prominent mid-slope fault offsets the seafloor up to ~350 m in seven seismic images, and multibeam bathymetry ties those fault images together in a series of cross sections across a ~100-km-long fault (Fig. 9). Differences in morphology on the upslope and downslope side of the fault indicate significant displacement prior to or during glacial erosion. Up-slope of the mid-slope fault, the Miocene shelf sediment section can be followed down the upper slope to water depths of 1–2 km (Winston, 1983; von Huene et al., 2012; Fig. 9). The Kodiak margin also hosts rare embayments in the shelf (numbered 1–5, Fig. A4). We have indicated glacial channels to distinguish these structures from the shelf embayments (Fig. A4). Embayments into the accreted prism are clearly younger than those farther upslope. GLORIA backscatter data (U.S. Geological Survey, 2011) reveal a smooth embayment seafloor in the accreted prism (Fig. 10, center, south of the vent location). A complex backscatter pattern along the middle slope, southwest of line 117, is consistent

with the rough morphology (northwestern section of Fig. 10). Lineaments trending at N60°E along the entire Kodiak margin are located along the BSFZ, and some of these host vent structures (Fig. 10; see Fig. 9 for vent location). These circular craters occur on round or elongated mounds ~3–6 km in extent. Venting fluids were indicated locally by conductivity, temperature, and depth (CTD) measurements (Suess, 1994) along the 1964 southern Kodiak aftershock region seaward of the BSFZ.

Seismic Studies (Wide-Angle and Multichannel) of the Albatross Area

Variable Structure of the Seemingly Smooth Incoming Plate

The density of MCS data in the Albatross area is greater than along any other segment of the Alaska margin, and it includes two OBH transects. The incoming plate sediment layer is ~3 km thick at the deformation front (line 8, Fig. 5), and here, the plate interface depth is constrained by wide-angle (WA) reflection and refraction data with P-wave velocities ranging from 1.7 to 3 km/s. Where constrained by MCS tomography (line MGL15, Fig. 6B and line 117, Fig. 7B), seismic P-wave velocities of the incoming sediment locally show low-velocity zones in the gradually increasing velocities of sediment between the plate interface and oceanic basement. This velocity structure is most clear near the deformation front above subducting seamounts and their trailing flanks (line MGL15, Fig. 6B). Seismic P-wave velocities range from 4.3 to ~7.0 km/s in the oceanic basement of the incoming plate (Figs. 6B and 7B). The average sediment cover of ~3 km (e.g., on lines 117–120, Figs. 7 and 11), increases to 4.5 km thickness at the deformation front on lines 111 (Fig. 11C) and 119 (Fig. 11D). The position of the plate interface and top of the oceanic crust are constrained by both WA (Fig. 5) and coincident MCS data (Figs. 6, 7, and 11) to at least 30 km downdip of the deformation front. The shallow part of the subducting plate interface dips 4° (Fig. A5). Typical oceanic crustal seismic P-wave velocities increase downward to the Moho, which is ~14 km

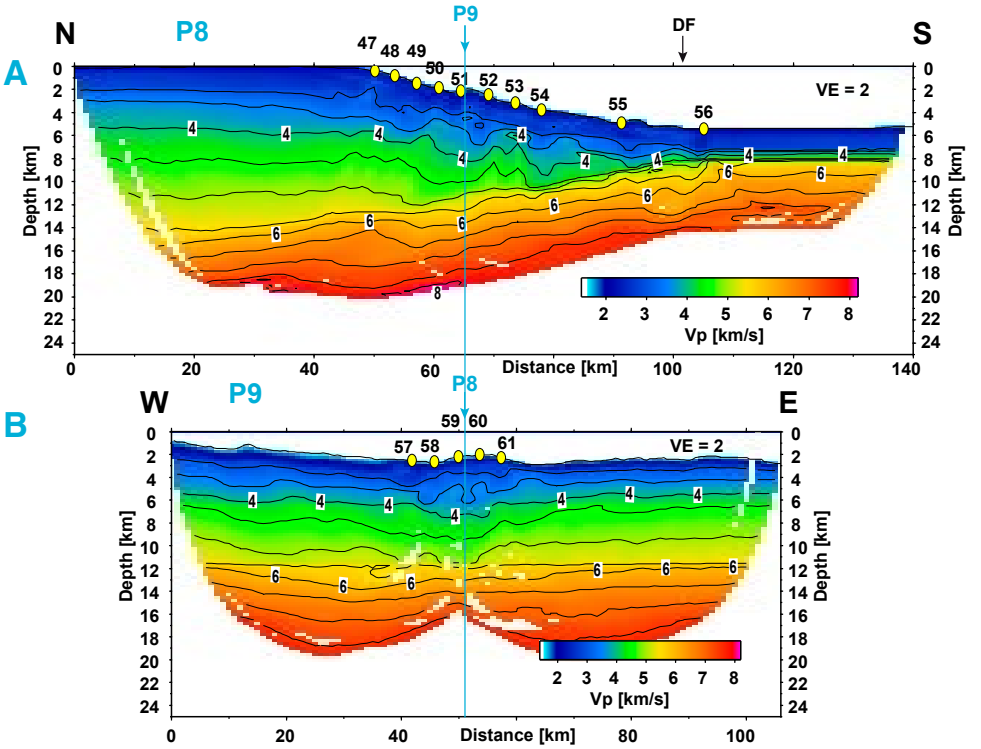

Figure 5. Final velocity models of (A) line P8 and (B) line P9 of wide-angle tomography with Tomo2D using the Monte Carlo approach (Korenaga et al., 2000; Korenaga and Sager, 2012). Yellow numbered dots indicate OBH locations. Isolines indicate seismic P-wave velocity at 0.5 km/s interval (4 km/s and 6 km/s are annotated). Vertical blue line across panels (A) and (B) indicates crossing line of the perpendicular profiles.

deep at the deformation front. In contrast to the seemingly smooth incoming seafloor on the Pacific plate (Fig. 1), the seismic data reveal numerous subducted seamounts and ridges beneath the Alaskan margin. Along line 117, three seamounts of ~500 m relief occur beneath the trench axis, as well as ~10 km and ~20 km farther down the subducting basement (Fig. 7). In the subduction zone, the plate interface mimics the subducting oceanic basement relief in the region of the southeastern MCS lines 106, 117, and 111 (Figs. 7, 11C, 11D). The dimensions of the subducting seamounts range from ~0.5–~3 km height, and the smaller seamounts extend across ~5–10 km (e.g., lines 117, 106; Figs. 7 and 11D), while the larger and more complex subducting seamounts extend ~20 km across (e.g., line MGL15, Fig. 6). Where subducting seamount height exceeds ~1.5 km, the seamounts disrupt the subducting sediments and form the plate interface (from east to west in lines MGL15, 120, 111, just seaward of the deformation front, Figs. 6, 11A, and 11C). Additionally, the subducting seamounts >1.5 km height locally increase the seismic P-wave velocities along the plate interface. Across strike, reflectivity of the subducting plate interface is highly variable. The overall high reflectivity near the trench decreases downdip of the accretionary ridges (lines MGL15, 117; Figs. 6 and

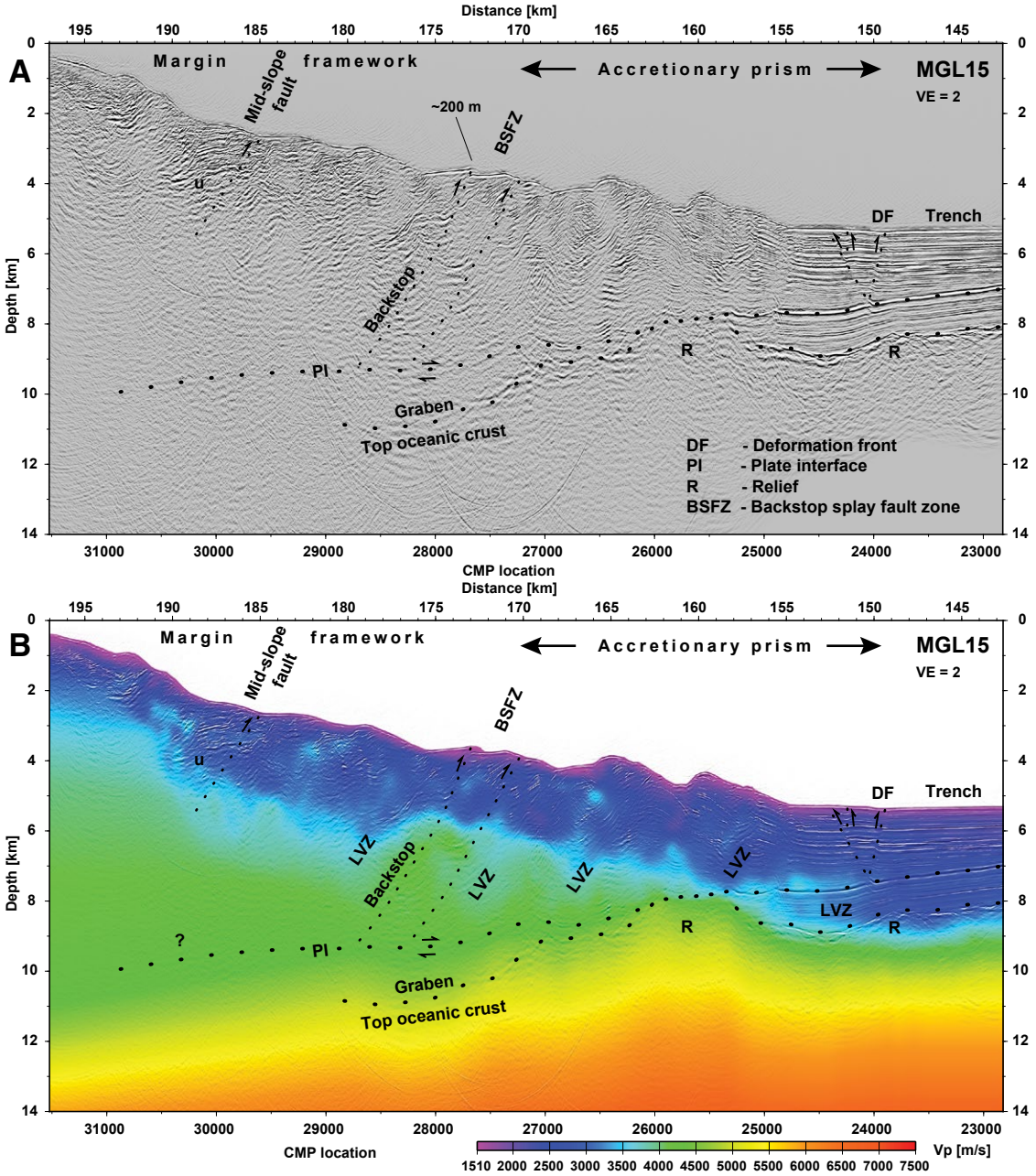

Figure 6. (A) Line MGL15 interpreted pre-stack depth migrated section applying the multichannel seismic (MCS)-traveltime tomography velocities. (B) Migration velocities on top of interpreted section. Plate interface and major thrusts are indicted by dotted lines. CMP—common midpoint; LVZ—low velocity zone; U—major unconformity; VE—vertical exaggeration. Landward subducting oceanic basement relief is associated with the subducting 56° fracture zone.

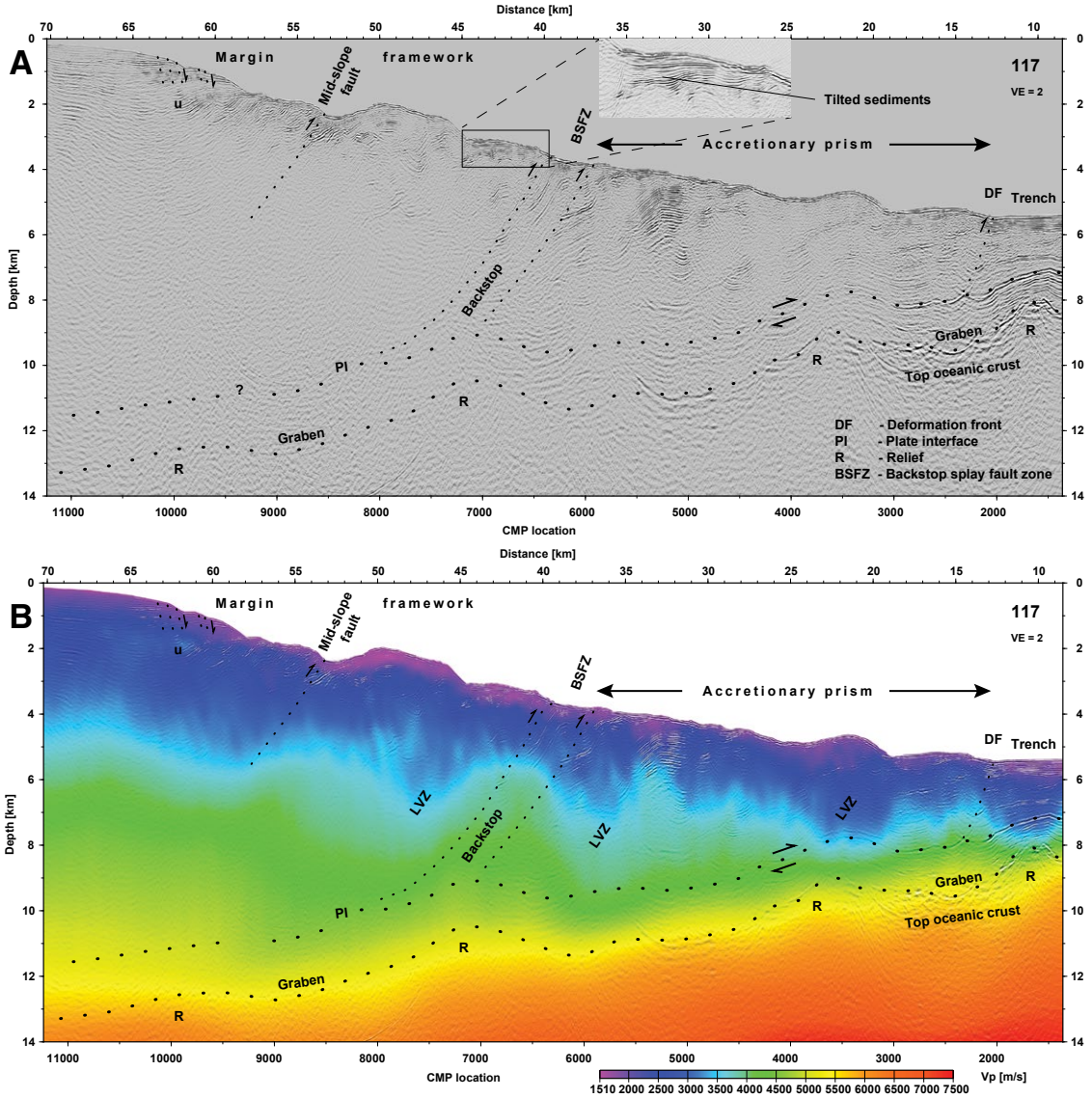

Figure 7. (A) Line 117 interpreted pre-stack depth migrated section applying the multichannel seismic (MCS)-travel-time tomography velocities. Inset shows landward tilted sediment on hanging wall of splay fault. (B) Migration velocities on top of interpreted section. Plate interface and major thrusts are indicated by dotted lines. CMP—common midpoint; LVZ—low velocity zone; U—major unconformity; VE—vertical exaggeration.

7). High-amplitude reflectivity on the plate interface occurs down to the junction with the BSFZ along lines 111 and 106 (Figs. 11C and 11D), and decreased plate interface reflectivity is observed where seamounts form the plate interface (lines MGL15, 120, Figs. 6 and 11A). Phase reversal of the highly reflective plate interface is locally observed (line MGL15, just seaward of the subducting seamount, Fig. 6A). Only the seamounts higher than 3 km, like those of the Kodiak and Bowie Seamount chain and the Patton and Murray Seamount chain, are resolved in existing bathymetric data covering the subducting Pacific plate (Fig. 1) and disrupt the sediment sequences at the deformation front. But even smaller seamounts, 1.5–3 km high above the oceanic basement and mapped along the northwestern MCS lines (e.g., in line 111 seaward of the deformation front, Fig. 11C, and lines 120, Fig. 11A, and MGL15, Fig. 6), impact the upper-plate structure by creating embayments into the deformation front (Fig. 9, Frederik et al., 2020).

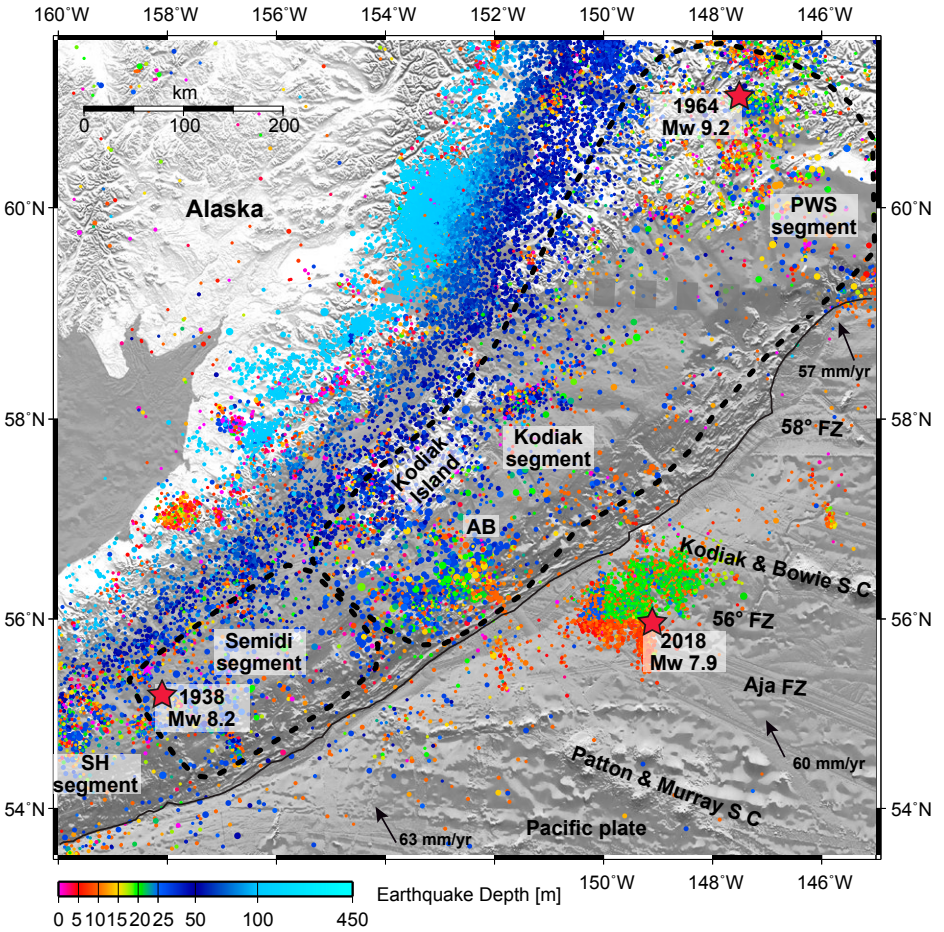

Figure 8. Map showing distribution of earthquakes of moment magnitudes Mw ≥ 2.5 since 1964 to January 2020 from the U.S. Geological Survey/National Earthquake Information Center (USGS/NEIC) earthquake catalog. Big red stars mark epicenters of the 2018 Gulf of Alaska complex oceanic crust and 1938 great and 1964 giant Alaska subduction megathrust earthquakes. Dashed circled areas show great and giant subduction rupture areas, rupture segments are annotated, and wide dashed gray line marks division of Prince William Sound and Kodiak segments. Earthquake depth is indicated by color code (note scale below) and magnitude by size of circles. PWS—Prince William Sound; FZ—fracture zone; SC—Seamount chain; AB—Albatross Bank; SH—Shumagin.

Along-strike variability is documented in two trench-parallel lines, 109 and 115 across the BSFZ and accretionary prism, located ~15 km landward of the deformation front and another, line 113, ~15 km farther landward along the middle slope crossing the inner forearc (Fig. 12). Many seamounts subduct beneath the lower slope, including smaller ones of ~0.5 km height and ~7 km across, and larger ones up to 2.5 km height and 10 km across. The depth of the oceanic basement varies between 9 and 11 km (lines 109 and 115, Fig. 12B) at ~15 km landward of the trench axis. The plate interface is located at depths of 7–9 km (lines 109 and 115, Fig. 12B). Again, as seen in the downdip direction (Figs. 6, 7, and 11), the plate interface mimics the oceanic basement relief above small subducting seamounts, whereas the large seamounts displace the subducting sediment (Fig. 12B). The plate interface reflectivity varies along strike, dividing the Albatross region into sections with high- and low-amplitude plate interface reflectivity. High-amplitude reflections with local reverse polarity occur in the southwest (SW of line 111, Fig. 12B), except for the region crossing line 106. Low-amplitude chaotic or non-coherent plate interface reflections occur northeast of line 111 (Fig. 12B).

Accretionary Prism, Inner Forearc, and Distinctive Fault Zones

The accretionary prism in the Albatross region displays well-stratified sedimentary layers (Fig. 12B). The middle slope strata are subhorizontal northeast of line 111, and large tilted sediment blocks are offset by deep thrust faults in the

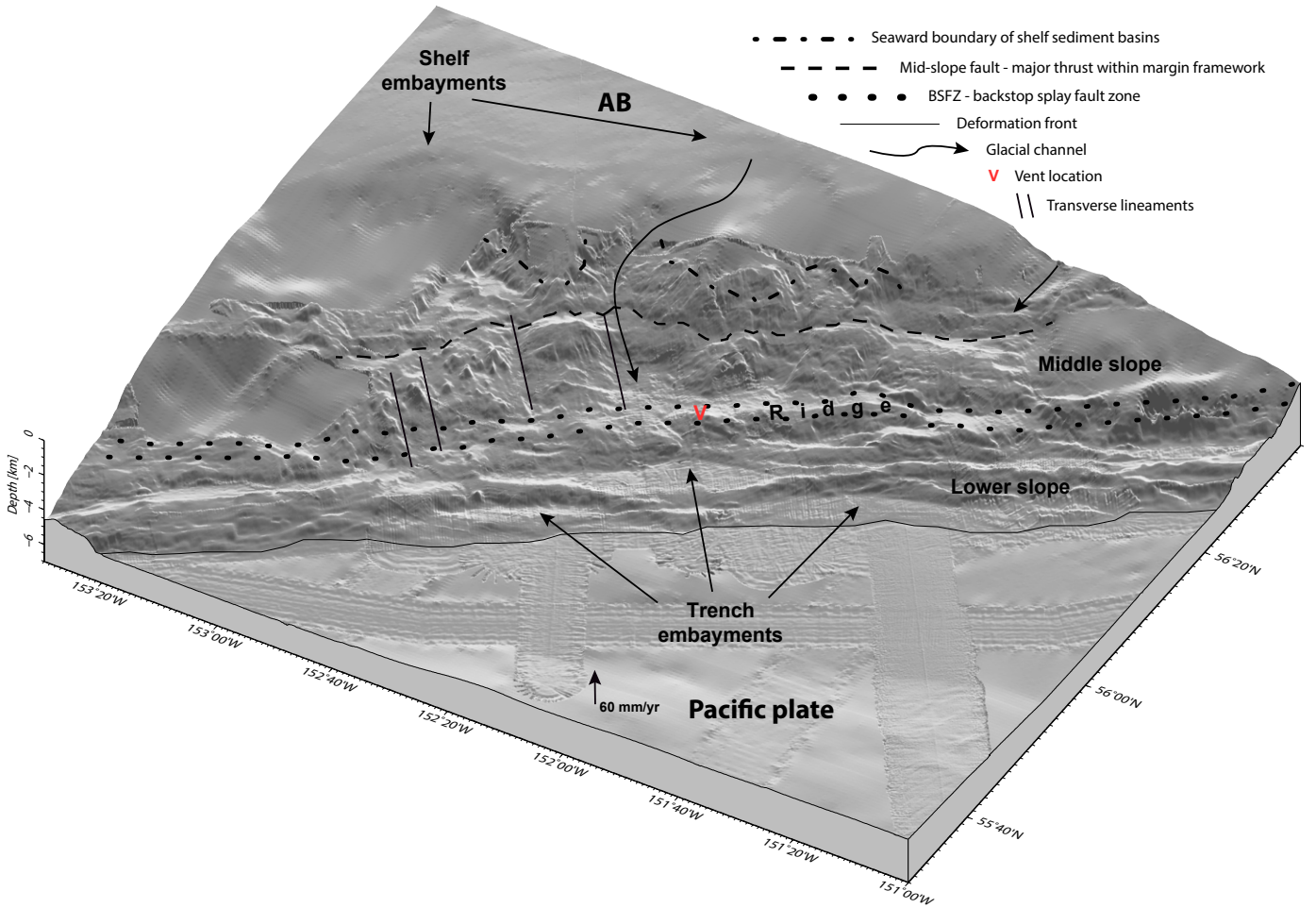

Figure 9. Interpretation of major along-strike structures on bathymetric perspective view of the Albatross region in the southern Kodiak segment of the 1964 earthquake rupture. Upper dotted-dashed lines are an approximation of the downslope extent of the shelf sediment section. Dotted lines outline the backstop splay fault zone (BSFZ), which marks a change in slope and structure in seismic images. A major mid-slope fault scarp is indicated by the dashed line, which is controlled by both seismic images and bathymetry. Glacial channels are shown to distinguish them from subduction-related morphological structures. AB—Albatross Bank.

northeastern part of the strike line image (line 113, Fig. 12A). In seismic dip lines, growth of the accretionary prism begins with proto-thrusts seaward of the deformation front beneath the trench floor. Most of these proto-thrusts branch off the plate boundary above positive relief in the underlying oceanic crust (seamounts), as prominently imaged in line 111 (Fig. 11C). In line MGL15, the oceanward progression of accretionary prism structure advances with emergence of the proto-thrust through the seafloor (Figs. 6 and 9).

The accretionary prism seismic P-wave velocity structure reveals patches of low velocity (LVZ in Figs. 6B and 7B) subparallel to the general trend of major thrust faults and increased seismic P-wave velocities (from 3 to 4.3 km/s) in the BSFZ region. In the ~15–20-km-wide accretionary prism (Figs, 6, 7, and 11), seismic P-wave velocities increase downdip above the subducting seamount in MGL15 (Fig. 6B) compared with lower seismic P-wave velocities above subducting sediment along

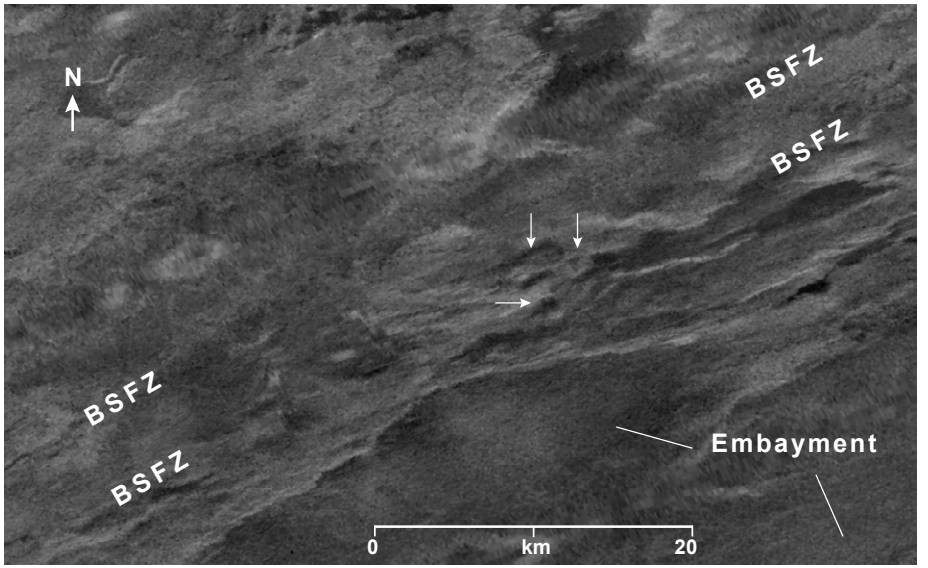

Figure 10. GLORIA backscatter data (U.S. Geological Survey, 2011) of mounds and vents (marked by white arrows) in the backstop splay fault zone (BSFZ) of the Albatross region. Note lineaments that are truncated by the BSFZ. Bar scales are approximate. Location shown with a red V in Figures 9 and 13.

the plate interface in line 117 (Fig. 7B). However, all P-wave seismic images of subducting seamounts show increased velocities at the leading edge and reduced velocities above and in the trailing flank (Figs. 6B and 7B). The most prominent thrust fault zone verified with bathymetry (Fig. 9) and residual bathymetry (Bassett and Watts, 2015) is along the BSFZ. The BSFZ is a listric splay fault zone (Figs. 6, 7, 11, and A5) that branches from the plate boundary at ~9 km depth. The splay fault zone dips ~60° and displaces the seafloor hundreds of meters, e.g., ~200 m on line MGL15 (Fig. 6). Hanging-wall sediment sequences behind the BSFZ (e.g., on line 117, Fig. 7 inset) are tilted, indicating repeated displacement. This set of splay faults forms the ~5–10-km-wide BSFZ transition that separates coherent accretionary prism reflections from a landward zone of more diffuse reflectivity. The 3.5° average slope angle of the accretionary prism increases at the BSFZ to 6° along the middle slope before decreasing to 2° on the shelf (Fig. A5). The BSFZ forms a ridge at the transition from the accretionary prism to the continental slope (Figs. 6 and 11). Some of the BSFZ faults branch upward from the subduction interface relief (i.e., seamounts in lines 111 and 117, Figs. 7 and 11). The small-wavelength seafloor roughness that characterizes bathymetry of the middle slope differs from that of the smoother accretionary prism (Figs. 9 and A5).

Another distinct thrust fault extends across the Albatross region (Fig. 9); the fault cuts through the middle slope and dips ~60°, which we call a mid-slope fault (Figs. 6, 7, 11, and 12). The mid-slope fault offsets the seafloor up to ~350 m and is imaged to ~4 km depth below the seafloor (e.g., line 119, Figs. 11 and A4). Several normal faults dip seaward and cut through the upper slope and shelf of the Albatross region at the seaward end of the shelf sediment and its underlying unconformity (lines, 119, 120, 706, Fig. 11). The normal faults are imaged a few hundred meters to ~1 km depth below the seafloor. Normal faults offset the seafloor locally up to ~100 m and the tilted strata indicate block rotation (lines 106/706, 119, Fig. 11).

DISCUSSION

The tectonic deformation in the Albatross area is of particular interest because it is the site of a large amount of aftershock activity following the 1964 earthquake (Fig. 8, Ichinose et al., 2007). The extent of the Albatross MCS network enabled the construction of 2.5D maps showing plate interface and oceanic basement isodepths (Fig. 13). The subducting plate relief in the context of other geophysical data reveals the interconnection of upper-plate structure with the plate interface and oceanic basement relief. Structural characteristics of the 1964 southern Kodiak aftershock region are illustrated in the schematic Figure 14. The following discussion starts with the structure of the incoming plate, its impact on the plate interface properties and on the upper-plate structure, starting at the deformation front and progressing landward across the accretionary prism and the middle slope. The role of the BSFZ and the mid-slope fault are discussed, ending with structures along the upper slope and shelf edge. Finally, we speculate on how the presence of significant structural features affects the seismic cycle.

Impact of Incoming Oceanic Basement Relief on Plate Interface Morphology

Seamount subduction significantly affects morphology, structure, and vertical motion in subduction zones and also impacts the probability of large earthquakes (e.g., Watts et al., 2010). Whether the subduction of smooth or rough ocean crust is correlated with the size of earthquakes has been argued for decades (e.g., Ruff, 1989; Scholl et al., 2015). The subducting Pacific plate at the Alaska subduction zone is considered a smooth example by various authors from which a smooth megathrust fault is generally inferred (e.g., Wang and Bilek, 2014; Lallemand et al., 2018). Smooth megathrust faults are thought to be favorable for great and/or giant earthquakes (e.g., Wang and Bilek, 2014; Scholl et al., 2015; Lallemand et al., 2018; Geersen, 2019). However, we find that the igneous crust of the subducting Pacific plate is not as smooth as

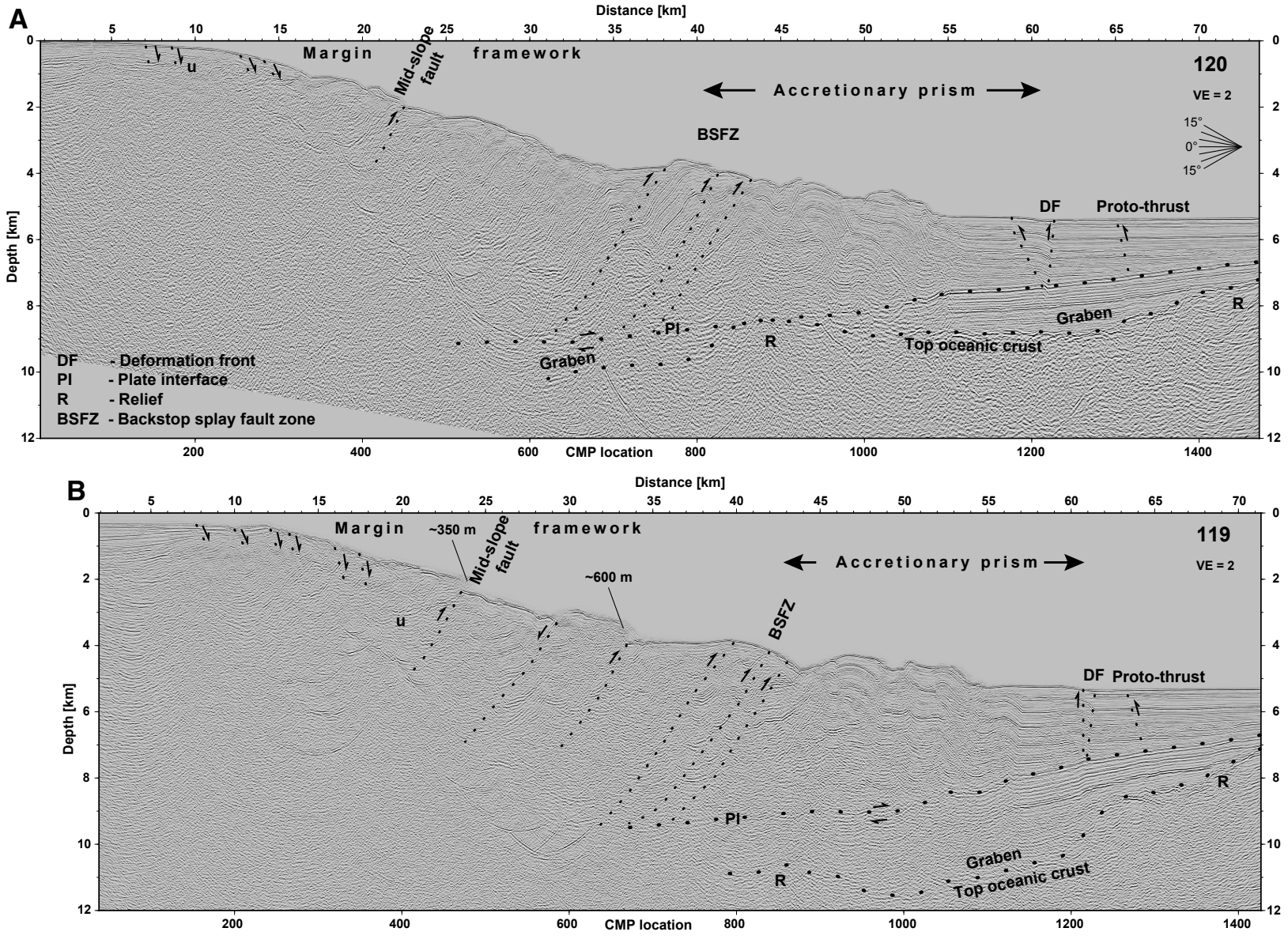

Figure 11. From east to west: (A) Line 120 interpreted pre-stack, depth-migrated multichannel seismic (MCS) section. (B) Line 119 interpreted pre-stack depth migrated MCS section. (C) Line 111 interpreted pre-stack depth migrated MCS section. Proto-thrusts branch from a buried seamount. Due to the currently subducting graben, sediment thickness here is ~4 km at the deformation front. (D) Line 106/706 interpreted pre-stack, depth-migrated MCS section. Plate interface and major thrusts are indicted by dotted lines. Note normal faults in the upper slope; CMP—common midpoint; U—major unconformity; VE—vertical exaggeration. Landward subducting oceanic basement relief in lines 120 (A) and 119 (B) are associated with the subducting 56° fracture zone. (*Continued on following page.*)

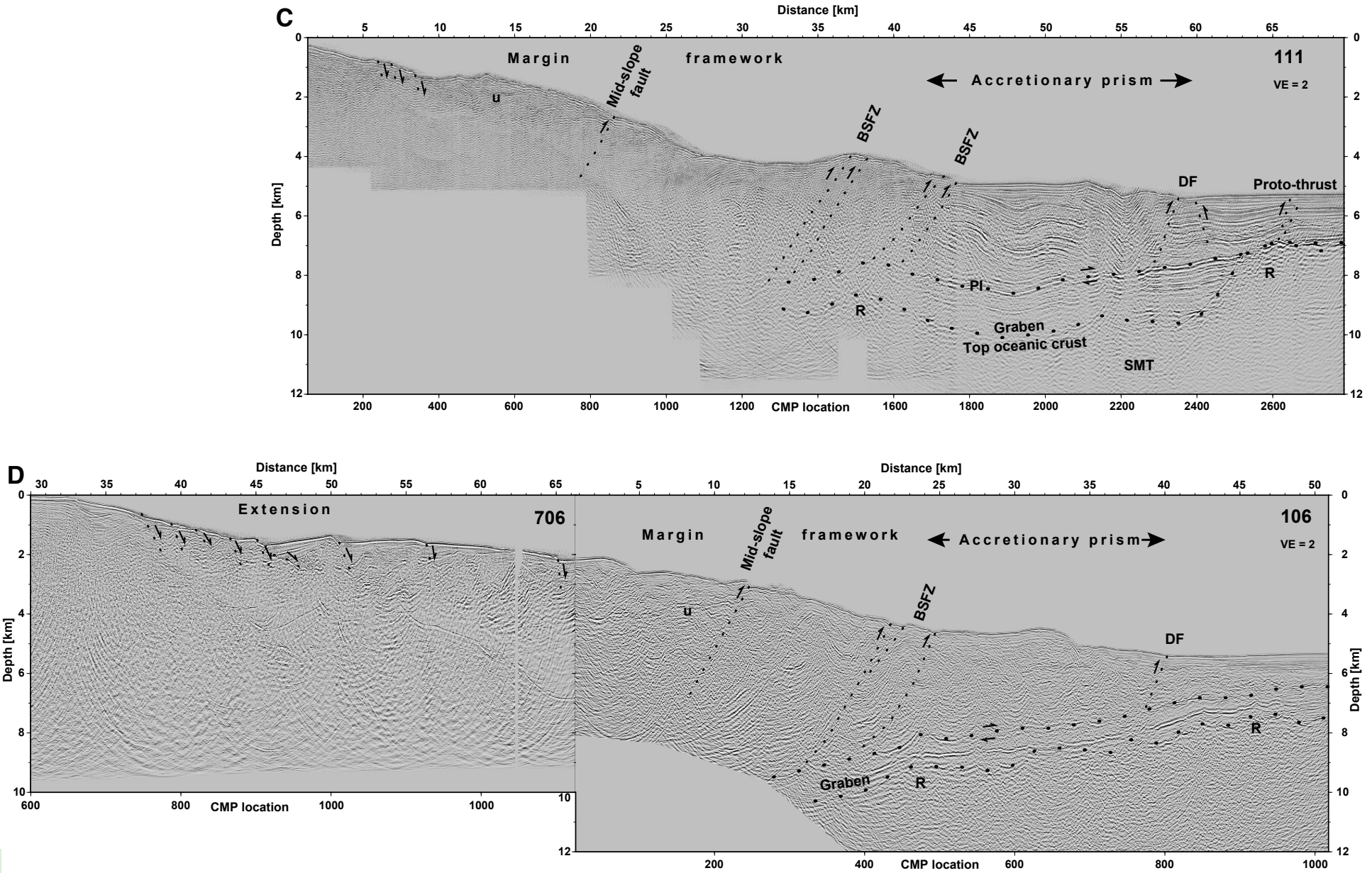

Figure 11 (*continued*).

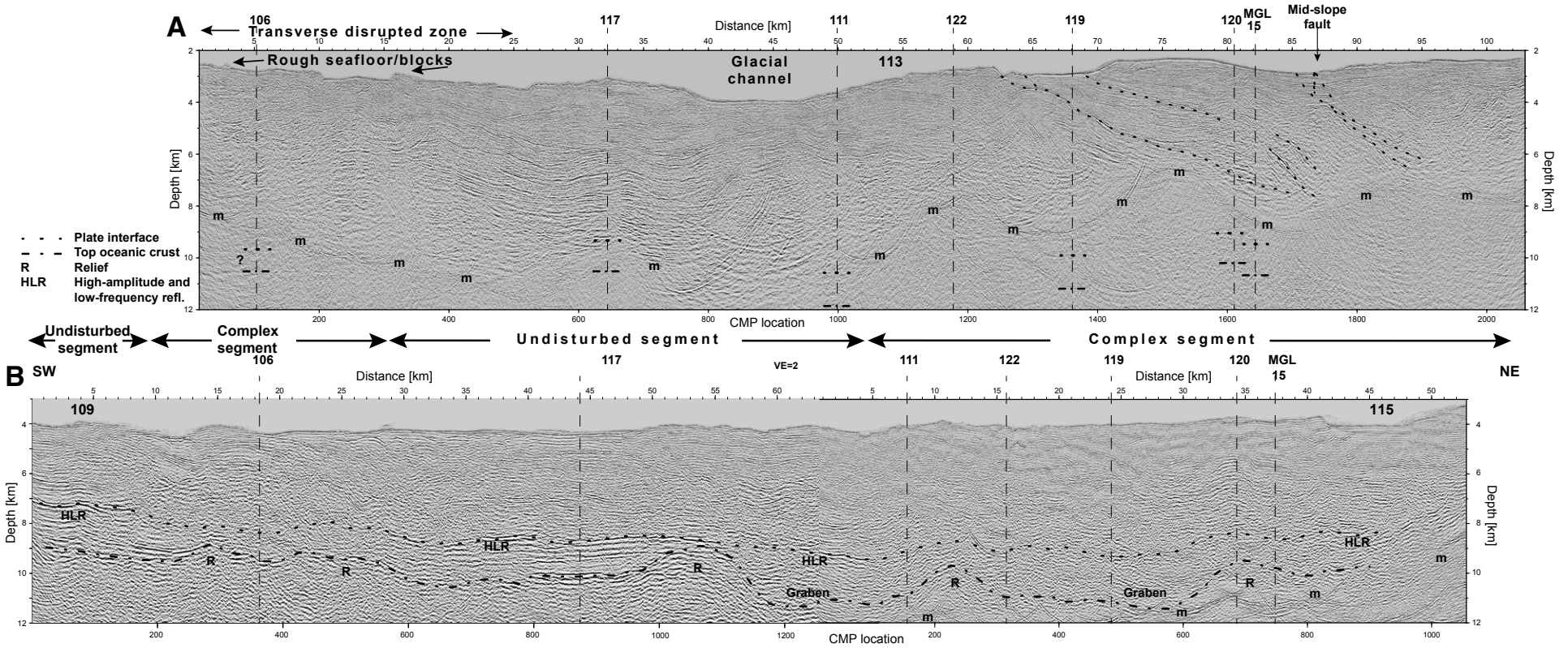

Figure 12. Interpreted pre-stack, depth-migrated multichannel seismic (MCS) sections trending along-strike in the lower and middle slope. (A) Middle slope line 113 and (B) merged lines 109 and 115 across the lower slope. Dashed vertical lines show locations of crossing lines. Plate interface and oceanic crust picked on crossing profiles are indicated by dotted lines ~8–10 km depth. In line 113, the plate interface is obscured by the seafloor multiple, denoted m. The tectonic character differs between these strike lines, the one being on or near the backstop splay fault zone (BSFZ) and the other across the middle slope. CMP—common midpoint; HLR—high-amplitude and low-frequency reflections; VE—vertical exaggeration.

the seafloor bathymetry might suggest (Figs. 1 and A4). Thick, well-stratified sediment layers on the Pacific plate from high rates of glaciomarine sediment deposition formed the Surveyor fan (Stevenson and Embley, 1987; Reece et al., 2011; Gulick et al., 2015). The fan conceals rough topography of the igneous oceanic basement. Long-wavelength seafloor ridges entering the trench between the Kodiak and Bowie Seamount chain and Aja fracture zone have a subtle bathymetric expression (Figs. 1 and A4) of an underlying fracture zone system (Naugler and Wageman, 1973; Atwater and Severinghaus, 1989), which ruptured during the rare 23 January 2018 Mw 7.9 earthquake in the incoming Pacific plate (Fig. 8, Krabbenhoeft et al., 2018). At the deformation front of the Albatross area, approximately two-thirds (2 km) of the incoming sedimentary section are accreted to the upper plate and one-third (~1–1.5 km) of the incoming sediment section enters the subduction zone (Figs. 6, 7, 11, and 12). Therefore, once subducted, the rough morphology of this fracture zone system is no longer moderated to the same extent by sedimentary cover. This allows large lower-plate heterogeneities to impact the plate interface. We propose that plate-bending related faulting observed in the outer rise region most likely adds additional roughness and/or heterogeneity to the subducting oceanic basement, as shown in the Shumagin segment of the Alaska margin (von Huene et al., 2019). Along the plate interface, continuous, high-amplitude and low-frequency reflections lose amplitude or continuity where seamounts occur, which leads

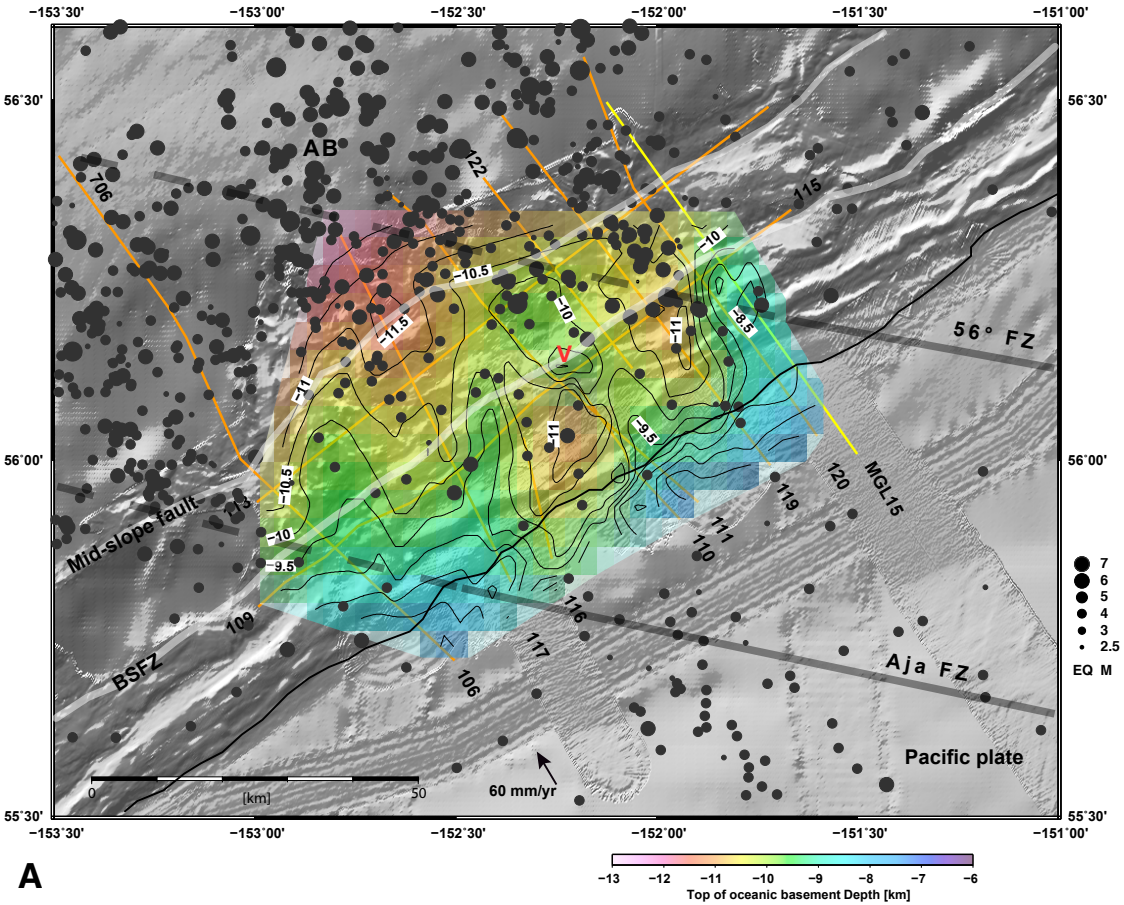

Figure 13. Superimposed oceanic basement (A) plate interface (B) depth plotted with isodepth contours (depth in km) on bathymetry. Solid black line marks Alaska trench axis. (A) Seismic lines are shown in orange—legacy multichannel seismic (MCS) and yellow—new MCS. Solid bold black lines show locations of major fracture zones; their landward continuation beneath the upper plate is marked by dashed black lines. Annotated white lines outline backstop splay fault zone (BSFZ) and mid-slope fault locations. (A and B) Earthquakes (black dots; since 1964 to January 2020; see magnitude-size relation in legend on the right; from U.S. Geological Survey/National Earthquake Information Center (USGS/NEIC) catalog (https://earthquake.usgs.gov/earthquakes/search.) and (B) numbered slip contours (dashed black) of the 1964 earthquake (after Ichinose et al., 2007; slip in meters). AB—Albatross Bank; FZ—fracture zone; V—vent site; EQ M—earthquake magnitude. (*Continued on following page.*)

to a downdip variability in plate interface properties (Figs. 6 and 11). Complex or well-stratified, high-amplitude and low-frequency plate interface reflections are influenced by subducting seamounts. Where subducting oceanic basement relief exceeds 2 km height, the plate interface reflections are commonly complex or chaotic. The seismic image of a chaotic and complex plate interface near subducting seamounts portrays permanent deformation and/or fluid depletion, in contrast to high-amplitude and low-frequency reflections (e.g., Fig. 6). Patterns of plate interface reflectivity also change along-strike. High-amplitude and low-frequency reflections and well-stratified subducting sediments are found east of line 106 and between lines 106 and 111 (Fig. 12). Lower amplitude and more chaotic reflectivity occur above rough oceanic basement topography showing the lateral variability along the plate interface (Fig. 12). The corresponding high (seamount) and low structures of the subducting fracture zone basement along lines MGL15 (Fig. 6), 119, 120, and 111 (Fig. 11, Krabbenhoeft et al., 2018) coincide with large variations in plate interface seismic P-wave velocities (Figs. 6 and 7). These spatial variations in P-wave velocity may indicate spatial variations in geological, thermal, and hydrologic conditions and could be a cause of heterogeneous frictional properties along the plate interface megathrust (Wang and Bilek, 2014). Along rough segments of the 1964 southern Kodiak aftershock region, subducting oceanic relief influences normal stress and seismic coupling locally along the megathrust. This could produce patches of greater strength compared with surrounding smooth sediments along the plate interface (e.g., Ruff, 1989; Bilek and Lay, 2002).

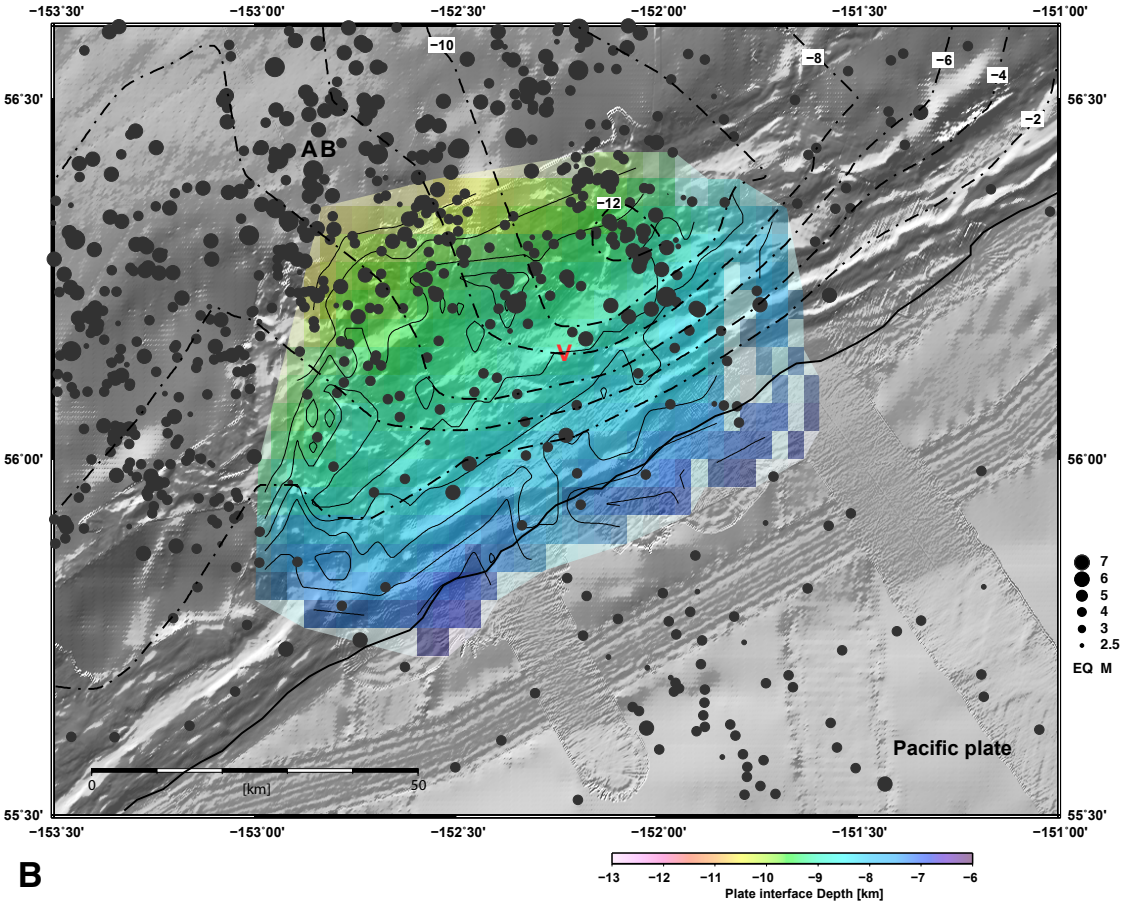

Figure 13 (*continued*).

Effects on the Upper-Plate Structure from Subducting Oceanic Basement Roughness

Subducting seamounts and fracture zones play an important role in tectonic processes of the upper plate and have influenced faults near the deformation front (Davis and von Huene, 1987). As proposed by Wang and Bilek (2011), subducting seamounts can produce fracture systems in the overriding plate that may extend rupture from the megathrust fault to the surface thus enlarging the earthquake magnitude and tsunami hazard (Wang and Bilek, 2011). Here, in the Albatross aftershock region, extensive fracture systems are related to subducting oceanic basement highs of seamounts and the irregular morphology of fracture zones.

The Trench

The initial stage of subduction along the Alaska trench involves well-stratified sediments that document the influence of subducting oceanic basement relief on the deformation of the sediments above and below the plate interface. The >3-km-thick sediments play an important role in moderating effects of the subducting oceanic basement relief (Fig. 1). Faulting and fractures observed in the upper plate may document deformation above subducting oceanic basement highs (e.g., below the plate interface at the deformation front in lines MGL15, 119, Figs. 6 and 11B). In the leading (landward) flank of the subducting seamount in line 111 (Fig. 11C), a clear example of fractures, proto-thrusts, and deformation of the overlying sediments above a subducting oceanic basement

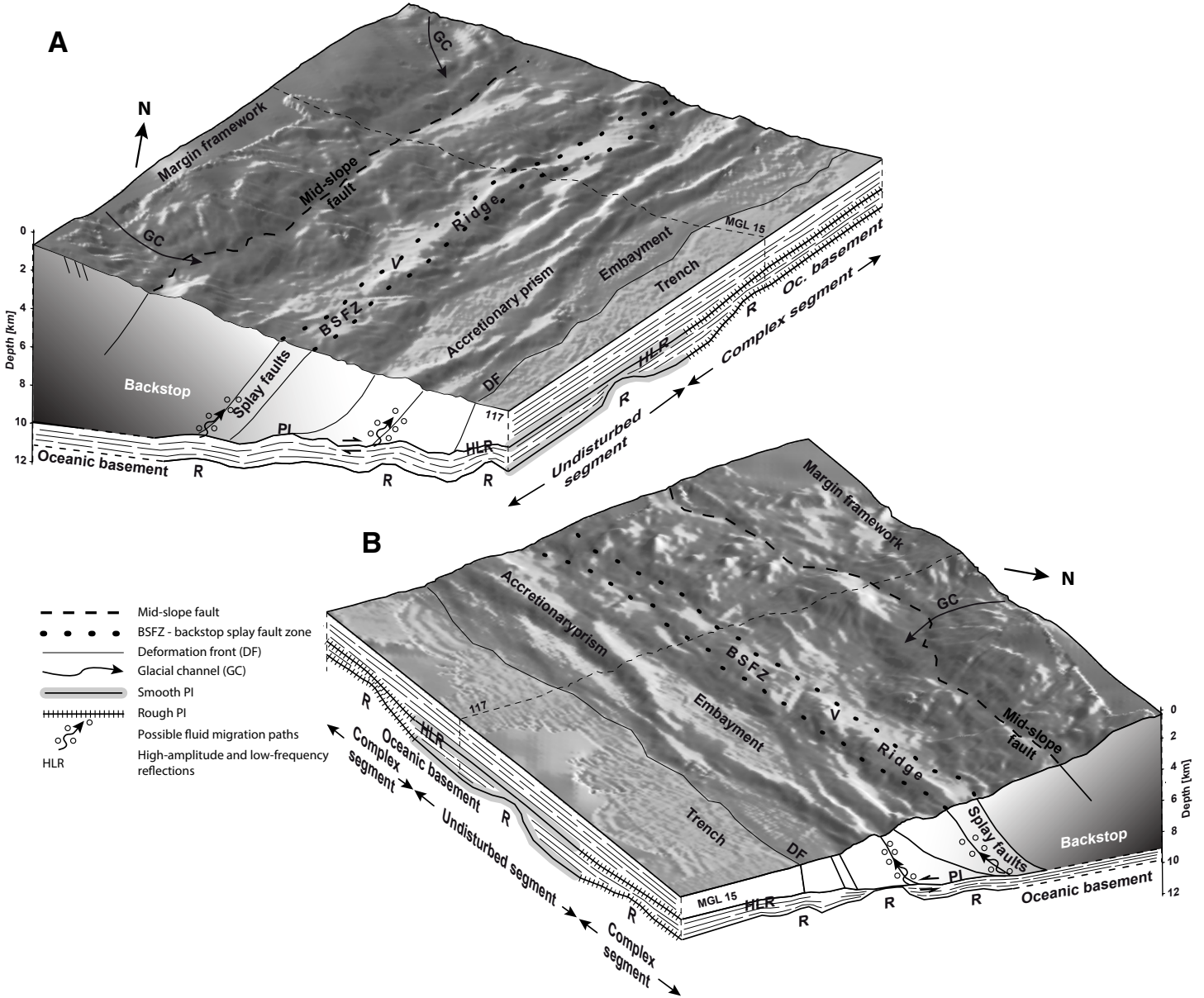

Figure 14. Schematic perspective views looking to the northeast (A) and southwest (B). Characteristic elements are shown with interpretation of representative seismic lines 117 and MGL15. Lower-plate relief is approximated on all seismic images. Upper-plate structure is complex above rough plate interface, whereas upper-plate structure is little disturbed above smooth plate interface. Thick sediment layer on the lower-plate smooths effects from rough oceanic basement. Open circles with wavy arrows mark possible fluid migration paths. BSFZ – backstop splay fault zone; DF—deformation front; GC—glacial channel; HLR—high-amplitude and low-frequency reflections; PI—plate interface; SMT—seamount; V—vent site; R—relief.

high are clearly displayed in well-stratified incoming sediments. This observation is consistent with the P-wave velocity distribution near the subducting seamounts (Figs. 6B and 7B). The above observed fault and P-wave velocity distribution above subducting seamounts are consistent with enhanced compression and increased development of upper-plate faults at its leading edge and relative extension in the wake of a subducting seamount in recent numerical models (Sun et al., 2020). In contrast, in the seismic lines located farther to the east, proto-thrusts have evolved in the otherwise well-stratified incoming sediments with no deformation above a smooth, high-amplitude and low-frequency plate interface reflection (e.g., line 120, Fig. 11). Proto-thrusts document a seaward growth of contractional deformation as observed elsewhere.

The Accretionary Prism

At shallow depths, subducting seamounts can cause seafloor uplift, which is commonly observed in other subduction zones, including Costa Rica (Harders et al., 2014). This process is sometimes accommodated by fracturing (Wang and Bilek, 2014) in conjunction with elastic flexure of the upper plate. In the Albatross aftershock region, seafloor uplift is not noticeable (Figs. 11–13), and clear bulges are not observed above subducting seamounts. Subducting sediment above the rough oceanic basement can moderate the influence of basement roughness on the overriding plate, plate interface morphology, and seafloor uplift. Nevertheless, in the accretionary prism, the reduced seismic P-wave velocity (LVZ, Figs. 6B and 7B) above and in the trailing (seaward) flank of subducting seamounts indicates increased porosity and thus under-consolidation in a subducting seamount "shadow zone" that is consistent with numerical modeling (Sun et al., 2020). Embayments occur along the lower slope (Figs. 9 and 13), where subsidence may occur in the wake ("shadow zone") of large subducting seamounts and fracture zones (Frederik et al., 2020). Besides these spatially and temporally limited erosional processes, accretion predominates along the lower slope, maintaining the ~15–20-km-wide accretionary prism taper.

Analog modeling has illustrated fracturing of the upper plate above subducting seamounts (e.g., Dominguez et al., 1998). Similar to these models, extensive fracture systems above subducting seamounts are imaged in high-resolution bathymetric data off Costa Rica (Harders et al., 2014). In the Albatross accretionary prism, the absence of small-scale fractures in the multibeam bathymetric images above subducting seamounts may stem from lower resolution of the 1990s multibeam imaging systems available as well as lack of fractures in 1980s GLORIA backscatter data (Fig. 10). The seismic P-wave velocity model and seismic reflection interpretation reflect the complex structure of the accretionary prism. Multiple landward-dipping imbricate thrust faults rooting at the plate interface form a ~15–20-km-wide accretionary prism (Figs. 6, 7, and 11). The landward steepening of the imbricate thrust faults (e.g., double BSFZ in line 111, Fig. 11C), documented by tilted sediment layers (inset, Fig. 7), indicates permanent shortening of the accretionary prism landward of the deformation front. The orientation and spatial distribution of seismic P-wave velocity anomalies, interspersing blocks of higher and lower seismic P-wave velocity units in the pattern of imbricate thrusting, suggest a causal link between them. Faults associated with imbricate thrusting in accretionary frontal prisms may provide a pathway for pore fluids liberated from subducting sediments and igneous crust by dehydration processes, as suggested for other subduction margins (Nicaragua—Sahling et al., 2008; Costa Rica—Ranero et al., 2008; Bangs et al., 2015; Barbados—Bangs et al., 1999; Hikurangi, New Zealand—Crutchley et al., 2020; Nankai—Tobin and Saffer, 2009). This inference is consistent with venting through the accretionary prism seaward of the BSFZ (venting structures in backscatter data, Fig. 10) and possibly to the trench axis of the Alaska margin observed by Suess et al. (1998).

In the accretionary prism, above the leading flank of subducting seamounts (Figs. 6 and 7), reduced reflectivity (Figs. 6, 7, and 11 the downdip seamount in line 111) and elevated seismic P-wave velocities may indicate reduced porosity and possible over-consolidation and advanced dewatering of sediment. These geophysical results are consistent with Deep Sea Drilling Project (DSDP) drill cores at a site off central Kodiak Island (Lee and von Huene, 1973), subsequently shown to overlie a subducting seamount. Material from cores 340–369 m below seafloor were abnormally dewatered and consolidated to a vertical effective stress of more than 10^6 pounds per square foot (47.88×10^6 N/m^2) or equivalent to a maximum of ~5 km below seafloor (Lee and von Huene, 1973). The reduced seismic P-wave velocities in the upper plate and accretionary prism above and in the trailing flank of subducting seamounts suggest possible extension and elevated sediment porosity. These interpretations are supported by numerical modeling of hydromechanical effects of seamount subduction (Sun et al., 2020).

Along-strike variation across the lower slope of the accretionary prism exhibits a mixture of deformation styles. Complex internal structure above a chaotic, low-amplitude plate interface contrasts to well-structured, mainly horizontally layered sediments in the upper plate above a high-amplitude and low-frequency plate interface reflection (Fig. 12). Here, we propose that along-strike variations in upper-plate tectonic deformation and seismic P-wave velocity structure are influenced by changes in subducting plate interface roughness.

The Backstop Splay Fault Zone (BSFZ)

The major role in subduction zone dynamics that splay faults play has only recently been appreciated (e.g., Moore et al., 2007), and structures that are probably splay faults have not yet been described as such in the Albatross aftershock region. Here, the most prominent set of splay faults form a BSFZ (Figs. 6, 7, 9–11). Hanging-wall tilted sediment sequences (e.g., inset, Fig. 7) show the periodic BSFZ landward rotation and uplift. The rough seafloor topography above the BSFZ (e.g., faults trending parallel to the BSFZ in the backscatter image, Fig. 10) and the hanging-wall seafloor offset of the Albatross BSFZ (e.g., ~200 m, Fig. 6) suggest recent displacement. The BSFZ coincides

with a lateral increase in seismic P-wave velocities and constitutes a transition zone sandwiched between the accretionary prism domain of imbricate thrusts and the poorly coherent reflectivity beneath the middle slope. The lateral increase in the horizontal gradient of seismic P-wave velocities, associated with the BSFZ ridge (Fig. 9) and the change in reflection pattern across it, also indicate a higher rigidity of the landward lithology compared with the more recently accreted prism. The structural characteristics (plate interface subduction and slope angles, similar take-off depth at plate interface, water depth, distance to the trench, associated landward seismic P-wave velocity increase, and distinct ridge) of the BSFZ at the prism to inner forearc transition (Fig. A5) make it a consistent feature of the Albatross area. From this BSFZ persistence along strike (Fig. A5), we conclude that although variability of lower-plate basement topography and plate interface roughness is large, this incoming plate heterogeneity may not influence construction of the BSFZ structure itself. An exception is where the leading flanks of subducting seamounts impact the BSFZ, locally amplifying the BSFZ ridge (Figs. 13A and A6). The plate interface is clearly a floor for complex faulting in the prism along the BSFZ.

Regional Considerations

This study of the Albatross area is related to similar ones that report BSFZs along the Alaska margin (von Huene et al., 2020, and references therein). The first tsunami earthquake was recognized in studies of the 1946 Unimak event at the southwestern end of the Alaska margin (Kanamori, 1972). The resulting tsunami was the largest ever generated during instrumental recording of earthquakes along the Alaska margin. The possibility of slip on the BSFZ in 1946 has been proposed from multibeam bathymetry around the epicenter (von Huene et al., 2016) near an MCS and wide-angle transect (Lizarralde et al., 2002). Farther northeast, a BSFZ is recognizable from Kodiak Seamount to Middleton Island (59.5°N) in studies of seismic images and bathymetry (von Huene et al., 2020). The continuation of the BSFZ from Middleton Island to the Unimak Islands raises the possibility that it may facilitate rupture across Alaskan megathrust segment boundaries.

Middle-Slope Fault and Extensional Faults of the Upper Slope and Outer Shelf

Middle-slope reflections, across the central part and on either side of the glacial channel, are subhorizontal and well stratified (Fig. 12A, line 113, km 20–60). In contrast, reflection patterns in the southwest and northeast ends of the line are deformed. Faults dominate the northeastern segment (Fig. 12A, northeast of km 60) and dip 10°–20° NW. The deformed strata above the seafloor multiple (echo of seafloor reflector) and the major faults are collocated above the leading flanks of two subducted seamounts, where clusters of aftershocks are observed (Figs. 13 and A6). Line 113 (Fig. 12A) demonstrates the mid-slope along-strike variability, which is influenced by the subducting plate structure (Fig. A6).

The prominent mid-slope fault extends more than 100 km along-strike ~35–40 km landward of the trench axis (Figs. 9 and A5). Its landward dip and hanging-wall offset in seismic images indicates reverse faulting. We infer the continuation of this mid-slope fault below the seafloor multiple at ~4 km depth (below sea level, e.g., Figs. 11 and 12, line 113) down to the plate interface because of its current seafloor offset of up to ~350 m along the hanging wall (line 119, Fig. 11) and its lateral extent across the Albatross region. The morphology of such a long fault is not reported from any other area along the Alaska margin and may be unique to the Albatross region; however, it was not recognized until the multibeam survey was examined.

The occurrence of shelf embayments in the landward continuation of significant subducting oceanic structures such as fracture zones and ridges (Fig. A4) suggests their causal correlation similar to the interconnection between subducting seamounts and the shelf embayments observed at the Costa Rican margin (Husen et al., 2002). Farther landward of the mid-slope fault, tectonic deformation becomes extensional along the entire Albatross region, as shown by normal faults and tilted blocks indicating rotation (best documented in line 106/706, Fig. 11). Potential sources of stress that explain such extensional regimes include uplift associated with seamount subduction, subduction erosion processes (Delouis et al., 1998; Sallarès and Ranero, 2005), variations in deformation through the seismic cycle (Loveless et al., 2005), or adjustments in wedge geometry (Loveless et al., 2010, and references therein). The major mid-slope thrust fault bounds the largely compressional regime seaward of the fault from the extensional regime in the upper slope and shelf region. We suggest the mid-slope fault plays a major role in deformation of the upper plate, based on its fault geometry and large dimensions (laterally and at depth). Considering the growth of the accretionary prism along the Alaska margin, the major mid-slope thrust fault possibly displays an earlier stage of BSFZ across the Albatross region, which shifted seaward during subduction of relief and subsequent accretion of the Alaska margin.

The Relation of Variable Incoming Oceanic Basement Roughness and Upper-Plate Significant Structures with the Seismic Cycle

Numerical modeling (Sun et al., 2020) and observations in several subduction zones (e.g., North Hikurangi margin—Todd et al., 2018; Southern Japan—Mochizuki et al., 2008; Ecuadorian margin—Martínez-Loriente et al., 2019) show small earthquakes cluster in the leading edge of subducting seamounts. High rates of seismicity (Mw<7) following the giant Mw 9.2 1964 earthquake in the southern Kodiak aftershock region (Fig. 8) and a 1964 afterslip maximum (Suito and Freymueller, 2009) coincide with the active BSFZ structures of high 1964 slip (Figs. 1, 8, 13, Ichinose et al., 2007). Here, seismicity concentrates beneath the inner forearc and is scarce in the accretionary prism (Figs. 8 and 13). This pattern of seismicity indicates a highly heterogeneous distribution of frictional properties in the Albatross region as observed by Agurto-Detzel et al. (2019) along the Ecuadorian margin. Martínez-Loriente et al. (2019)

correlate the nucleation of the 2002 Mw 6.4 Costa Rica megathrust earthquake with the leading flank of a subducting seamount in the area of highest tectonic overpressure. The seismicity cluster in the Albatross region in the leading flank of subducting seamounts (Fig. 13 and MCS lines MGL15, 120, 111; Figs. 6, 11A, and 11C) suggests a similar correlation of upper-plate tectonic processes resulting from subducting seamounts along the plate interface. Seismicity concentrates where the subducting oceanic basement consists of graben structures indicating interseismic activity and is scarce above subducting seamounts, indicating interseismic quiescence. This evidence supports the hypothesis that the plate interface is locally smoothed by sediment above subducting grabens. The seismicity cluster at the leading edge of the subducting seamounts (Fig. 13A) show that slip is promoted where the megathrust fault strength is increased (in agreement with numerical models by Sun et al., 2020).

Generally, shallow rupture during great subduction zone earthquakes may be inferred by the occurrence of outer rise earthquakes (Sladen and Trevisan, 2018) due to stress accumulation and transfer during a seismic cycle in areas of highest seismic moment release (or highest slip) (Christensen and Ruff, 1983, 1988; Dmowska and Lovison, 1992). This in turn increases the tsunami hazard of the subduction zone (Kanamori, 1972). The 1964 giant Alaska megathrust event has not been identified as a tsunami earthquake (Kanamori, 1972). However, the above criteria apply to the 1964 southern Kodiak aftershock region. The maximum slip of the 1964 earthquake from central to the southern Kodiak shelf (Figs. 1, 8, and 13, Ichinose et al., 2007) and 1964 afterslip maximum (Suito and Freymueller, 2009) coincide with the active BSFZ structures (Figs. 6, 7, 11, and 13). Additionally, significant seismicity occurred and is still ongoing in the nearby outer rise region (Fig. 8). Numerical modeling of effects on tsunami generation (Wendt et al., 2009; Lotto et al., 2019) suggests that slip along a shallow-dipping main thrust is deviated into steeper-dipping, upper-plate faults in the presence of barriers (i.e., seamounts), rather than continuing rupture along the megathrust. Given the giant size of the 1964 main event in combination with the seismicity and stress distribution (Ichinose et al., 2007; Suito and Freymueller, 2009), modeling results (Wendt et al., 2009; Lotto et al., 2019; Sun et al., 2020), and the structure we derived from seafloor morphology and seismic images, we consider shallow coseismic slip during the 1964 giant megathrust earthquake likely. Our preferred scenario in the Albatross region is the slip redirection into the preexisting splays forming the BSFZ in the leading flank of subducting seamounts (Figs. 6, 7, and 13) instead of continuation along the shallow-dipping main thrust.

SUMMARY AND CONCLUSIONS

The Albatross high-slip rupture area of the 1964 southern Kodiak aftershock region was surveyed with a grid of seismic lines that approximate a 3D survey. The 1970s seismic data were reprocessed with current software, and together with multibeam bathymetry, P-wave, wide-angle velocity structure, and MCS tomography, they constitute a new data set for the investigation of subduction zone tectonics in Alaska. Regional GLORIA backscatter images (U.S. Geological Survey, 2011), vertical gravity gradients (http://topex.ucsd.edu, Sandwell et al., 2014), and earthquake epicenter compilations (https://earthquake.usgs.gov/earthquakes, http://www.aeic.alaska.edu/html_docs/db2catalog.html) are publicly available. A schematic perspective (Fig. 14) summarizes significant characteristics of the Albatross high-slip rupture area. Structural features seem related to the roughness of the subducting oceanic basement. The seismic grid permitted construction of 2.5D images (Figs. 13 and A6) allowing superposition on the subducting oceanic basement, the overlying plate interface, and 3D views of seafloor morphology. These show significant lateral variations in lithospheric structure of the incoming plate and tectonic deformation in the overriding continental margin.

The incoming Pacific plate has typical oceanic crustal seismic velocities. Abundant oceanic basement topography, including seamounts and fracture zones with dimensions of ~500 m to 3 km height and ~5–20 km across, is covered by ~3–5 km of thick glaciomarine sediment. While one-third (~1–1.5 km) of incoming sediments subduct, two-thirds (~2 km) are accreted to the upper plate. Once subducted, varying plate interface reflectivity, structure, and seismic P-wave velocities reveal varying physical properties across the plate interface, implying mixed deformation styles and possible varying frictional and hydrologic properties. Contrary to previous studies, we show the presence of an overall rough, highly varying plate interface related to subducting basement relief. The upper-plate imbricate thrust structure of the ~15–20-km-wide accretionary prism accommodates the area of highest shortening across the Albatross margin. Embayments into the accretionary prism are associated with seamount subduction. The backstop splay fault zone (BSFZ) is a ~5-km-wide, recently active transition zone. It separates the active accretionary prism (low P-wave velocity) from a less reflective middle prism with higher P-wave velocities. This BSFZ structure across the entire Alaska margin consists of listric splay faults that connect the plate interface with the seafloor.

Additionally, we infer a mid-slope fault, extending >100 km along strike and ~35–40 km landward of the deformation front. This forms a boundary between a more contractional regime downslope and extensional regime upslope, where normal faults prevail along the upper slope.

We find a correlation of subducting plate morphology, upper-plate tectonic structures, and earthquake distribution. An earthquake cluster coincides with the area of maximum slip of the 1964 giant Alaska earthquake. Indications for rupture of the shallow subduction zone may be outer rise aftershocks seaward of the area of highest coseismic slip of the 1964 southern Kodiak asperity, the nearby highest density of seismicity, and recent activity of the BSFZ inferred from the tectonic structure of the seismic images with seafloor offsets up to 200 m. Therefore, we consider slip extension of the giant 1964 Alaska megathrust rupture along the BSFZ to the seafloor possible. The BSFZ can be a powerful tsunami generator when earthquake slip travels up the BSFZ rather than along the plate interface. The acquisition of high-resolution multibeam bathymetric data along with the currently

deployed long-term seismic offshore instrumentation will help to better resolve structures related to subduction zone mechanisms with higher precision earthquake relocation. This, in turn, would further our understanding of subduction zone mechanics of possible future great earthquakes in the Alaska subduction zone.

APPENDIX

Seismic Data Analysis

A detailed description of the seismic wide-angle (WA) and multichannel (MCS) analysis is given below.

Wide-Angle Seismic Tomography

Wide-angle seismic data were acquired in 1994 during RV *Sonne* cruise 96 (Flueh and von Huene, 1994). Here, two perpendicular profiles were investigated in detail: 10 ocean bottom hydrophone (OBH) instruments were unequally distributed along the ~140-km-long trench-perpendicular profile P8 at an average receiver spacing of 4 km on the middle slope and ~13.5 km for the two southernmost OBHs on the lower slope and oceanic plate (Figs. 1 and A1). Five OBH instruments were distributed along the center of the ~105-km-long trench-parallel profile P9 at an average spacing of 3.5 km. The intersection of P9 at OBH 60 (at profile km 53) occurs on the middle slope with P8 at OBH 51 (at profile km 64.5, Figs. 5, A2, and A3). Sometimes two (and at other times one) 32 L air guns were shot at an interval of 60 s, which, at a ship's speed of ~3.2 kn, results in an average shot spacing of ~100 m. The seismic signal generated refractions across the entire lengths of the seismic transects (≥100 km/≥60 km offset from the OBH positions along P8/P9; see data examples, Figs. 2–4).

The OBHs recorded reflections and refractions of the sedimentary layers in the overriding upper plate as well as the oceanic lower plate (Figs. 2–4). Clear refractions of the crustal interface (Pup) of the upper plate as well as oceanic plate (Plp) constrain the lower-crustal seismic P-wave velocities. The plate interface reflection Ppi and also the Pn and PmPoc (mantle refractions and reflections of the subducting oceanic plate, respectively) recorded on some stations constrain the deep seismic P-wave velocities and plate geometry.

Uncertainties assigned to the manually picked traveltimes vary from 20 ms (for the well-constrained shallow refractions) to 100 ms (for the deep reflections of the oceanic crustal Moho) (PmP) and hard-to-identify far offset refractions (Pn on some OBHs)), depending on clarity of arrivals. The number of picks is given in Table A1.

The joint wide-angle seismic reflection and refraction tomography tomo2D (Korenaga et al., 2000) yields the 2D velocity-depth structure. Reflections are treated as floating reflectors from simultaneous inversion of first arrivals and reflection traveltimes. Forward ray-tracing uses the hybrid scheme based on the graph method (Moser, 1991) with local ray-bending correction (Moser et al., 1992). Because tomo2D (Korenaga et al., 2000) inverts only for one reflection at a time, we iteratively inverted the traveltime picks in a top-to-bottom approach within eight (P8) and six (P9) steps, starting with the shallow reflections, and inverted for the Moho reflection in the last iteration step. Each step consisted of five iterations, and the resulting data uncertainty is given in Table A2.

The χ^2 values of P8 for the reflection of top of the oceanic crust could be reduced with additional time-consuming tomography iterations without significantly improving the P-wave velocity model. Instead of increasing the tomographic iterations for each step, we used the statistical approach described in detail by Korenaga and Sager (2012) to obtain the final P-wave velocity depth model. Therefore, 90 randomly perturbed reference 2D seismic velocity models of the preliminary post-stack time migration of the coincident MCS line 117 were used as starting models. Perturbation wavelength was 4 km horizontally and 1 km vertically. The velocity grid dimensions are 140 km long and 30 km deep with a horizontal grid spacing of 0.2 km and vertically varying from 0.05 km at the top to 0.22 km at the base of the model. Correlation lengths and smoothing weights were chosen, so that model areas with poor data fits did not produce overly smoothed models and well-constrained model areas did not produce small-scale features. The derivative weight sum (DWS) calculated by ray tracing through the average model may be regarded as a proxy for the ray density (Toomey and Foulger, 1989). Our preferred final velocity models (averaged Monte Carlo iterations) are shown in Figures A2 (P8) and A3 (P9) along with the fit between picked and calculated traveltimes, the standard deviation, and DWS.

PSDM and MCS-Tomography of M.G. Langseth *Line 15*

MCS line MGL15 was recorded during cruise *RV Langseth* L-09-11-GA in 2011 using a 6-km-long streamer (Frederik, 2016, https://walrus.wr.usgs.gov/namss/survey/l-09-11-ga-mcs/). Common-image-point (CIP) spacing is 6.25 m. Processing of line MGL15 included multiple removal using prediction and subtraction of multiple arrivals enhancing the image of thrust faults and the reflections of the subducting plate especially in the middle slope. The (preliminary) final velocity structure was obtained after an iterative approach of performing a time migration, improving the velocity model using a velocity analysis based on a semblance analysis, followed by a Kirchhoff prestack depth migration (PSDM).

After performing the wide-angle tomography (see above) with the starting velocity model of the (preliminary) PSDM of line MGL15, the wide-angle tomography result was improved with the MCS-tomography of USGS legacy line 117 (see below), which then was used as input velocity model here for line MGL15 to obtain the final velocity model using MCS-traveltime tomography for velocity update between PSDM iterations. The final result of the PSDM (Fig. 6) reveals thrusts in the middle slope reaching down to the subducting oceanic plate.

PSDM and MCS-Tomography of USGS Legacy Line 117

We re-processed USGS legacy MCS data acquired by the USGS vessel Lee in 1981 (L-7-81-WG, line 117, available at https://walrus.wr.usgs.gov/namss/survey/l-7-81-wg/) including shot- and intra-shotgather interpolation, multiple removal, and PSDM. Shot- and intra-shotgather-interpolation increased the lateral (by four times) as well as the vertical resolution and significantly reduced spatial aliasing. CIP spacing of the 2.5-km-long streamer was reduced to 6.25 m. Multiple removal using prediction and subtraction of multiple arrivals effectively removed multiples in the shallow part of the profile (NW) revealing the sedimentary structure down to 4 km depth. Multiple removals in the middle slope enhanced the image of thrust faults and the reflection of the subducting plate.

The starting velocity model for the PSDM was the smoothed result of the wide-angle tomography of coincident profile P8. MCS traveltimes were picked on every eighth (every 50 m) non-hyperbolic, moveout-corrected CIP gather. With each iteration step, grid cell size was reduced to improve the resolution. The data-driven, MCS-traveltime tomography was used to iteratively update the velocity model to obtain the final PSDM after three inversion runs. The image of the final PSDM greatly improved the shallow structure and even reveals the subducting oceanic crust (Fig. 7).

ACKNOWLEDGMENTS

Original seismic and bathymetric data are available at https://walrus.wr.usgs.gov/namss/ and https://cmgds.marine.usgs.gov/,

TABLE A1. NUMBER OF PICKS ASSOCIATED WITH REFLECTION AND/OR REFRACTION PHASES USED IN THE TOMOGRAPHIC INVERSIONS ALONG WIDE-ANGLE SEISMIC LINES P8 AND P9

Picked phase	P8	P9
Upper-plate reflections and/or refractions	974/4136	583/2941
Top of oceanic crust reflection and/or refraction	1156/3318	–/1530
Moho reflection and/or Pn–oceanic mantle refractions	607/3063	1191/1537

TABLE A2. TRAVELTIME MISFITS AND FITS TO THE DATA (IN TERMS OF A CHI-SQUARED STATISTIC) FOR THE TOMOGRAPHIC INVERSIONS ALONG BOTH WIDE-ANGLE SEISMIC LINES P8 AND P9

Picked phase	Traveltime misfit (ms)	χ^2 P8/P9
Upper-plate reflections and/or refractions	30	1.3/1.3
Top of oceanic crust and Moho reflection	120–130	2.2/1.0
Top of oceanic crust and mantle refraction	120–130	2.0/1.1

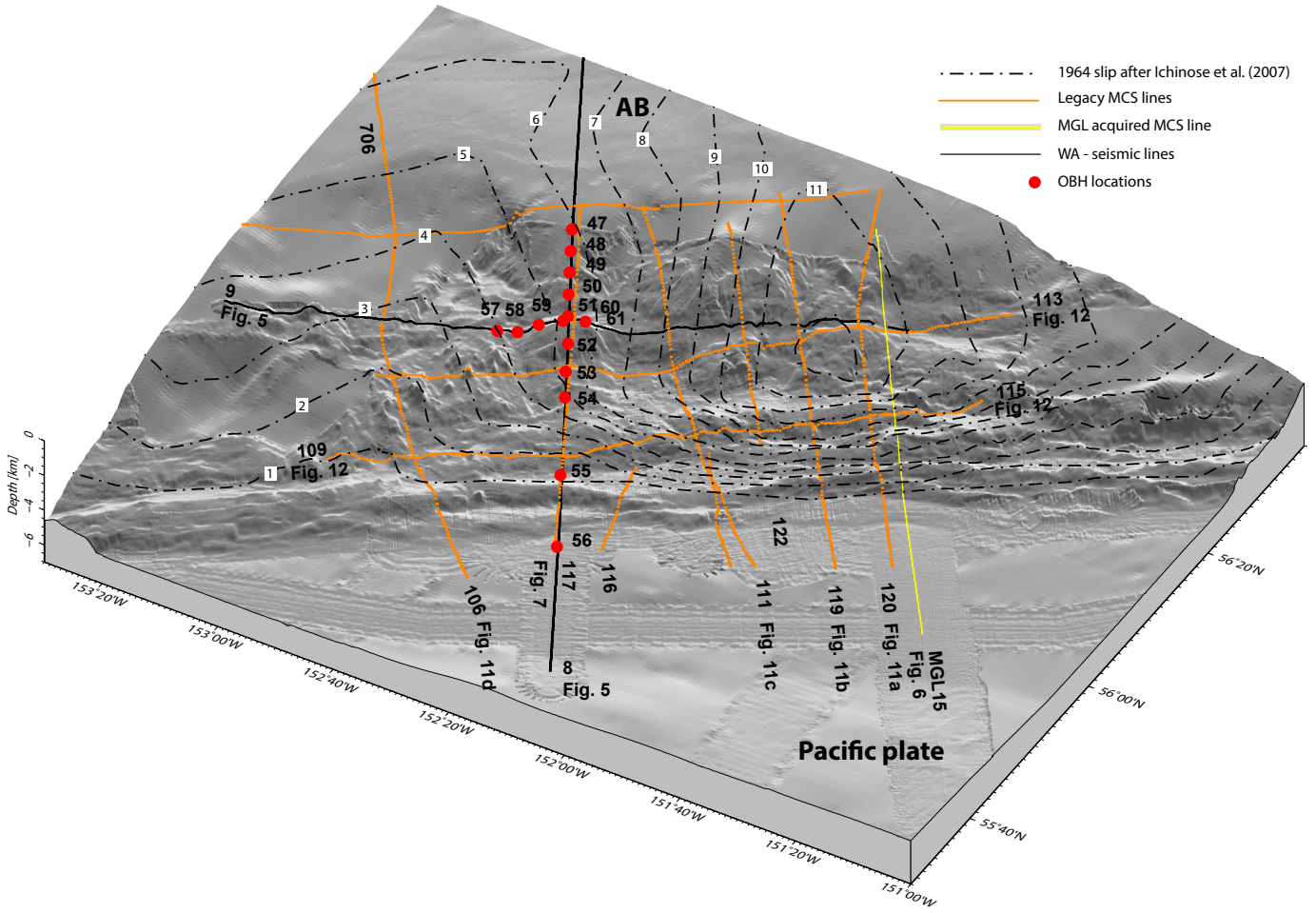

Figure A1. Bathymetric perspective view of the Albatross region in the southern Kodiak segment of the 1964 earthquake rupture. Seismic lines (orange—legacy multi-channel seismic [MCS]; yellow—new MCS; black—wide-angle), ocean bottom hydrophone (OBH) locations (red dots), and numbered slip contours (dashed black) of the 1964 giant earthquake (after Ichinose et al., 2007), slip in meters. AB—Albatross Bank. Seismic lines 116 and 122 were used for interpretation but are not shown in figures.

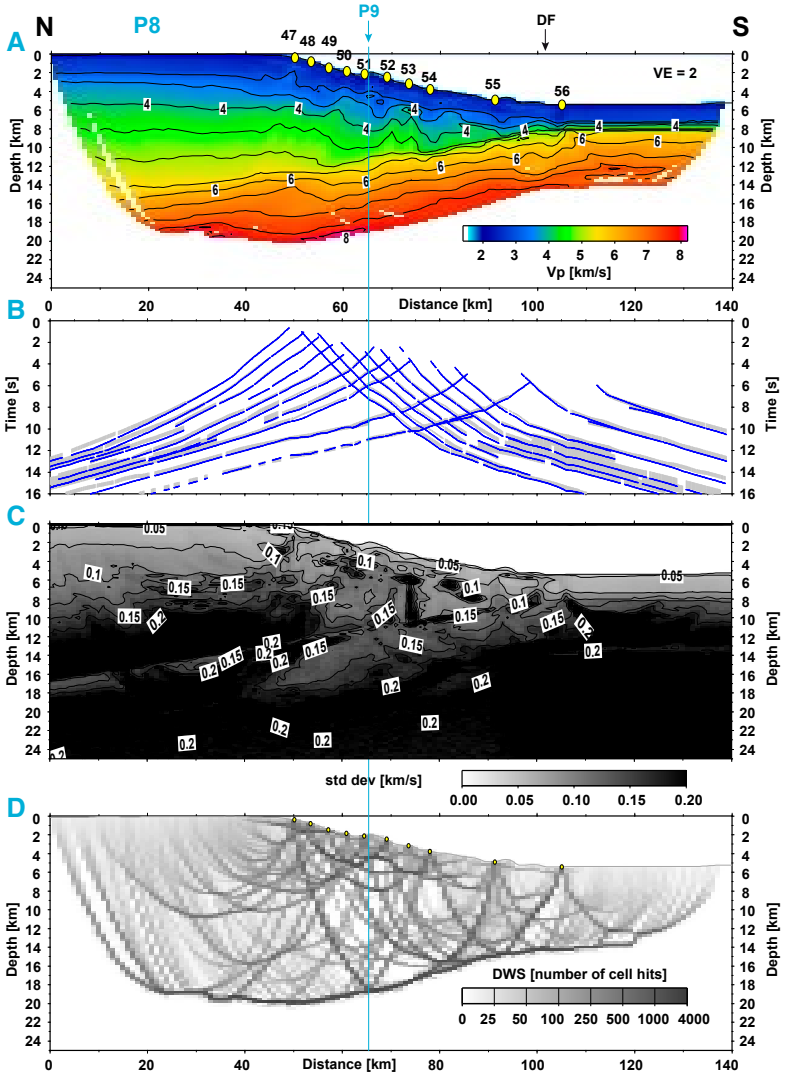

Figure A2. (A) Final velocity model of line P8 of wide-angle tomography with Tomo2D using the Monte Carlo approach (Korenaga et al., 2000; Korenaga and Sager, 2012). Yellow numbered dots indicate ocean bottom hydrophone (OBH) locations. Isolines indicate seismic P-wave velocity at 0.5 km/s interval (4 km/s and 6 km/s are annotated). (B) Picked (gray) and calculated (blue) traveltimes. (C) Standard deviation of final tomography. (D) Derivative weight sum (DWS) showing the ray coverage of final tomographic iteration. Blue solid line marks location of crossing line P9.

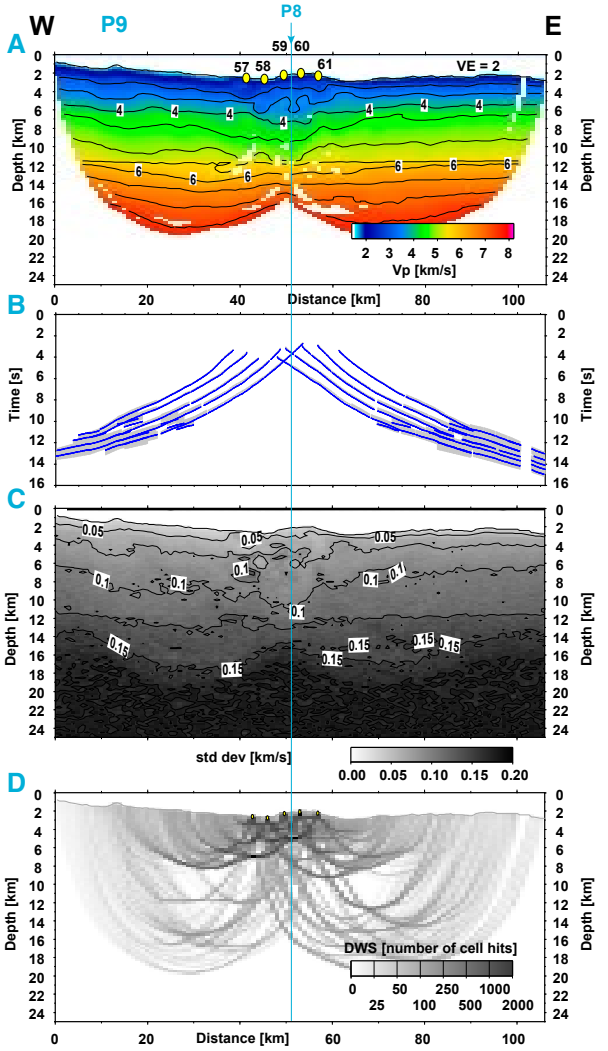

Figure A3. (A) Final velocity model of line P9 of wide-angle tomography with Tomo2D using the Monte Carlo approach (Korenaga et al., 2000; Korenaga and Sager, 2012). Yellow numbered dots indicate ocean bottom hydrophone (OBH) locations. Isolines indicate seismic P-wave velocity at 0.5 km/s interval (4 km/s and 6 km/s are annotated). (B) Picked (gray) and calculated (blue) traveltimes. (C) Standard deviation of final tomography. (D) Derivative weight sum (DWS) showing the ray coverage of final tomographic iteration. Blue solid line marks location of crossing line P8.

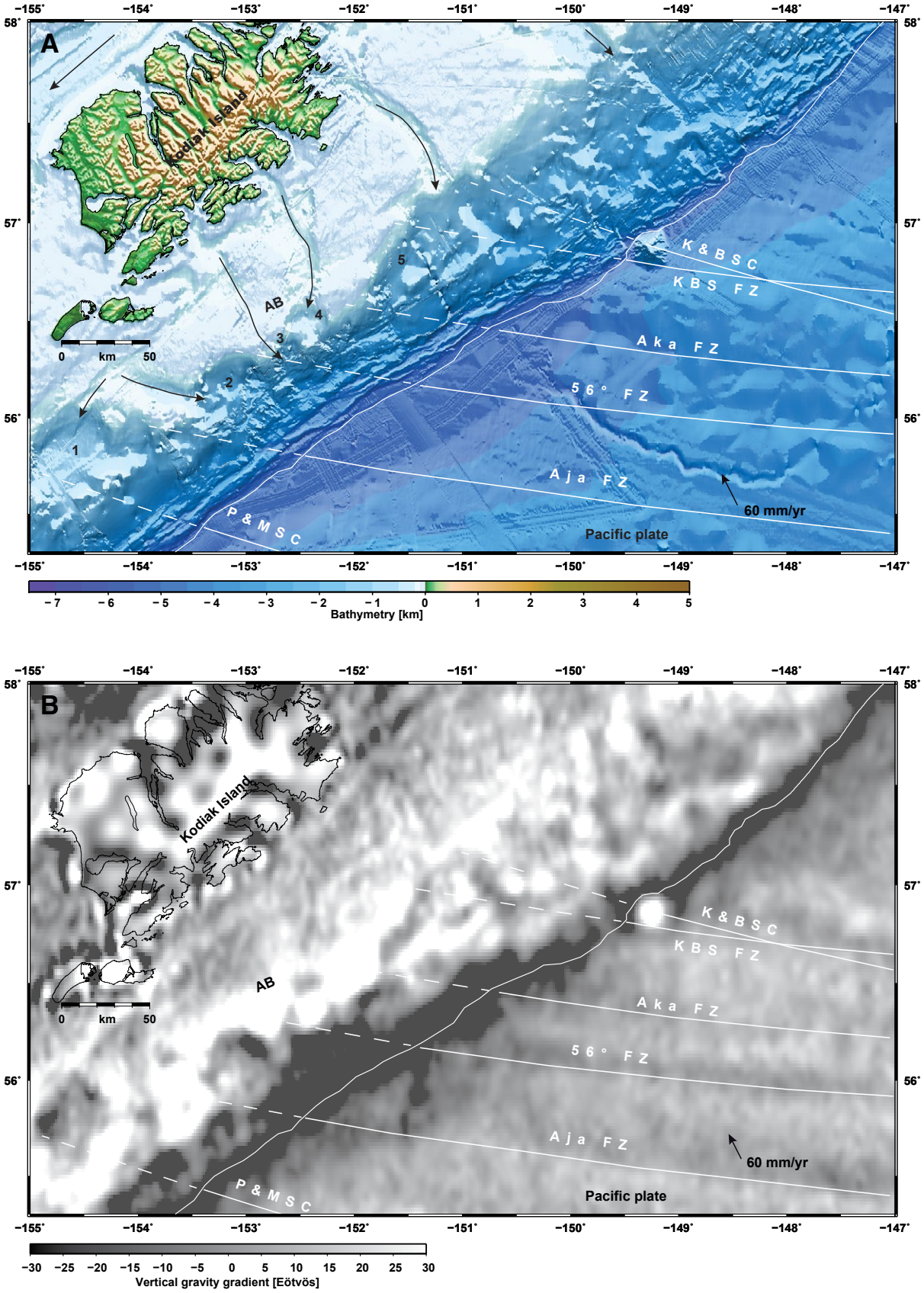

Figure A4. (A) Bathymetric map of the 1964 giant rupture across the southern Kodiak afterslip area. Shelf embayments are numbered. Black arrows follow glacial channels. (B) Map of vertical gravity gradient. White annotated lines, dashed in the continuation beneath the upper plate, show locations and trends of fracture zones and ridges. AB—Albatross Bank; FZ—fracture zone; K&BS—Kodiak and Bowie Seamount chain; P&MSC—Patton and Murray Seamount chain.

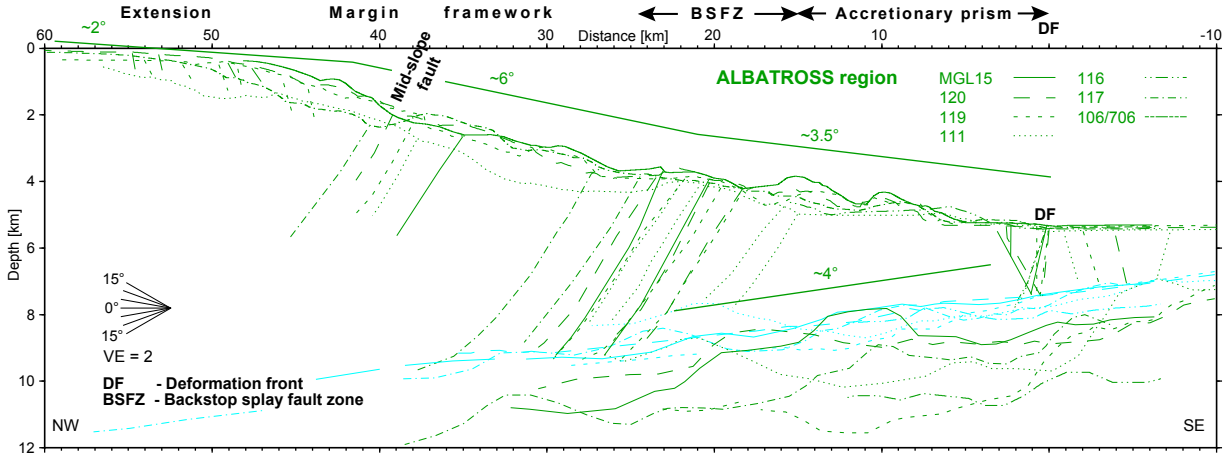

Figure A5. Alpha (α) versus β with backstop splay fault zone (BSFZ) of Albatross region. Seafloor with slope angle α, plate interface (light blue) with dip angles β, oceanic crust (green), and seaward thrusts of BSFZ and mid-slope fault picked from seismic lines. All angles denote average of all profiles. All profiles are aligned at the deformation front. Note uniformity of seafloor and location of the BSFZ and mid-slope fault.

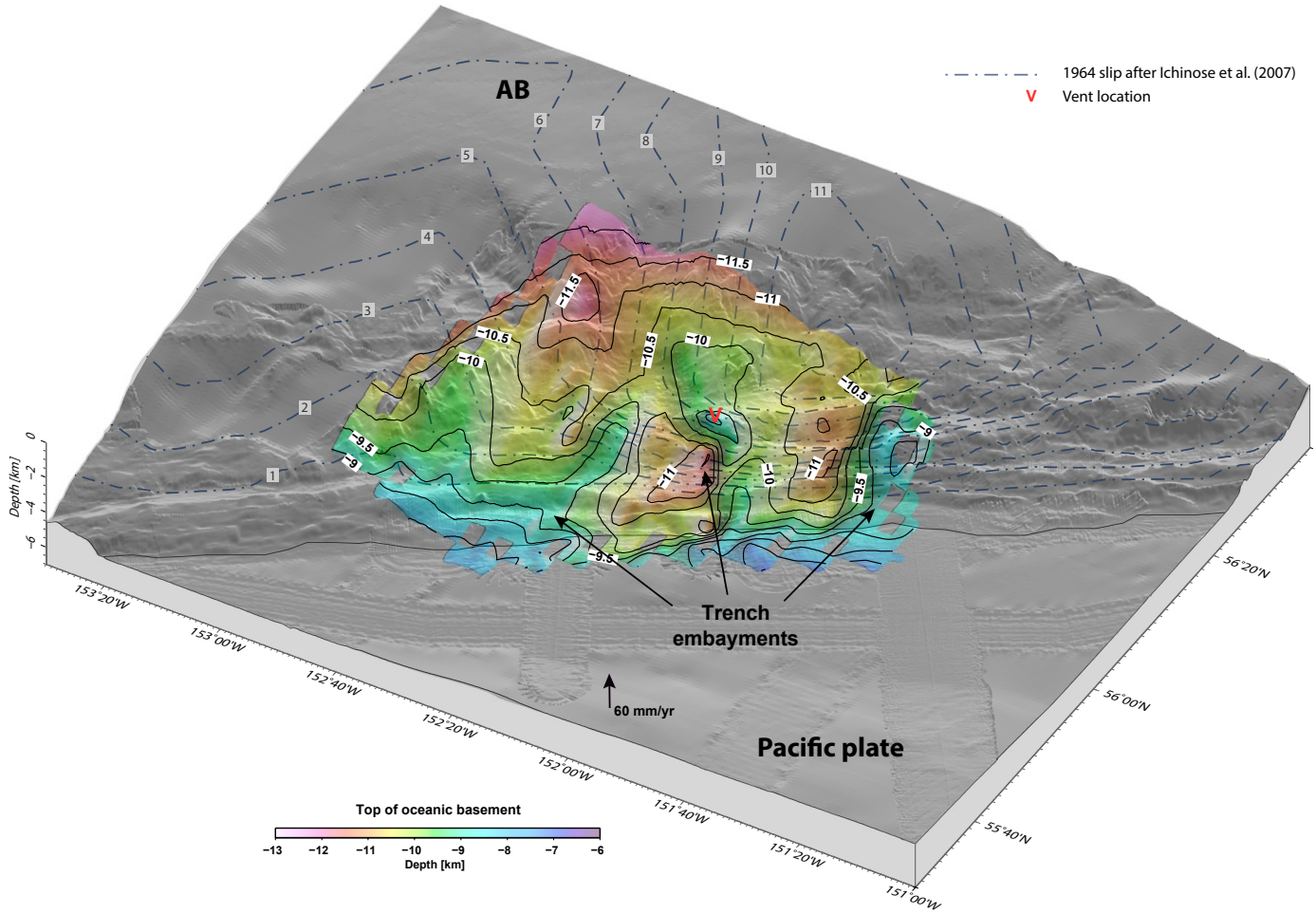

Figure A6. Bathymetric perspective view of the Albatross region in the southern Kodiak segment of the 1964 earthquake rupture. Numbered slip contours (dashed blue) of the 1964 earthquake (after Ichinose et al., 2007; slip in meters) and oceanic basement depth with solid, black, numbered isodepth lines are draped on bathymetry. AB—Albatross Bank.

respectively. Gravity data are available at http://topex.ucsd.edu (Sandwell et al., 2014). We acknowledge Sean Gulick, University of Texas at Austin, for the courtesy of providing line MGL15. The 1964 slip contours are from Ichinose et al. (2007). Omega2/Schlumberger, Seismic Un*x (Cohen and Stockwell, 2017) and ProMAX2D, Version 2003.19.1 (Halliburton, Inc.) were used for seismic data processing. Most of the figures were made with the Generic Mapping Tool (GMT) free software (Wessel and Smith, 1998). We thank Science Editor Shanaka de Silva for the handling of the manuscript during the review process. U.S. Geological Survey reviews by Samuel J. Heller, Ofori Pearson, and Janet Slate, the journal reviews of Guest Associate Editor Laura Wallace, Dan Bassett, and an anonymous reviewer greatly improved earlier versions of the manuscript. Any use of trade, product, or firm names is for descriptive purposes only and does not imply endorsement by the U.S. Government. AK was funded by the Deutsche Forschungsgemeinschaft, DFG, grant number KR3315/3-1.

REFERENCES CITED

Agurto-Detzel, H., Font, Y., Charvis, P., Régnier, M., Rietbrock, A., Ambrois, D., Paulatto, M., Alvarado, A., Beck, S., Courboulex, F., De Barros, L., Deschamps, A., Hernandez, M.J., Hernandez, S., Hoskins, M., León-Ríos, S., Lynner, C., Meltzer, A., Mercerat, E.D., Michaud, F., Nocquet, J.M., Rolandone, F., Ruiz, M., and Soto-Cordero, L., 2019, Ridge subduction and afterslip control aftershock distribution of the 2016 Mw 7.8 Ecuador earthquake: Earth and Planetary Science Letters, v. 520, p. 63–76, https://doi.org/10.1016/j.epsl.2019.05.029.

Atwater, T., and Severinghaus, J., 1989, Tectonic maps of the northeast Pacific, *in* Winterer, E.L., Hussong, D.M., and Decker, R.W., eds., The Eastern Pacific Ocean and Hawaii: Boulder, Colorado, Geological Society of America, The Geology of North America, v. N, https://doi.org/10.1130/DNAG-GNA-N.15.

Bangs, N.L., Shipley, T.H., Moore, J.C., and Moore, G.F., 1999, Fluid accumulation and channeling along the northern Barbados Ridge décollement thrust: Journal of Geophysical Research, v. 104, p. 20,399–20,414, https://doi.org/10.1029/1999JB900133.

Bangs, N.L., McIntosh, K.D., Silver, E.A., Kluesner, J.W., and Ranero, C.R., 2015, Fluid accumulation along the Costa Rica subduction thrust and development of the seismogenic zone: Journal of Geophysical Research. Solid Earth, v. 120, p. 67–86, https://doi.org/10.1002/2014JB011265.

Bangs, N.L.B., Moore, G.F., Gulick, S.P.S., Pangborn, E.M., Tobin, H.J., Kuramoto, S., and Taira, A., 2009, Broad, weak regions of the Nankai megathrust and implications for shallow coseismic slip: Earth and Planetary Science Letters, v. 284, p. 44–49, https://doi.org/10.1016/j.epsl.2009.04.026.

Bassett, D., and Watts, A.B., 2015, Gravity anomalies, crustal structure, and seismicity at subduction zones: 2. Interrelationships between fore-arc structure and seismogenic behavior: Geochemistry, Geophysics, Geosystems, v. 16, p. 1541–1576, https://doi.org/10.1002/2014GC005685.

Becker, J.J., Sandwell, D.T., Smith, W.H.F., Braud, J., Binder, B., Depner, J., Fabre, D., Factor, J., Ingalls, S., Kim, S.-H., Ladner, R., Marks, K., Nelson, S., Pharaoh, A., Trimmer, R., Von Rosenberg, J., Wallace, G., and Weatherall, P., 2009, Global Bathymetry and Elevation Data at 30 Arc Seconds Resolution: SRTM30_PLUS: Marine Geodesy, v. 32, no. 4, p. 355–371, https://doi.org/10.1080/01490410903297766.

Bilek, S.L., 2010, The role of subduction erosion on seismicity: Geology, v. 38, no. 5, p. 479–480, https://doi.org/10.1130/focus052010.1.

Bilek, S.L., and Lay, T., 2002, Tsunami earthquakes possibly widespread manifestations of frictional conditional stability: Geophysical Research Letters, v. 29, p. 1673, https://doi.org/10.1029/2002GL015215.

Bruns, T.R., von Huene, R., and Culotta, R.C., 1987, Geology and petroleum potential of the Shumagin margin, Alaska, *in* Scholl, D.W., Grantz, A., and Vedder, J.G., eds., Geology and resource potential of the continental margin of western North America and adjacent ocean basins—Beaufort Sea to Baja California: Houston, Texas, Circum-Pacific Council for Energy and Mineral Resources: Earth Science Series, v. 6, p. 157–190.

Byrne, D.E., Davis, D.M., and Sykes, L.R., 1988, Loci and maximum size of thrust earthquakes and the mechanics of the shallow region of subduction zones: Tectonics, v. 7, no. 4, p. 833–857, https://doi.org/10.1029/TC007i004p00833.

Caress, D.W., and Chayes, D.N., 1996, Improved processing of Hydrosweep DS multibeam data on the R/V Maurice Ewing: Marine Geophysical Researches, v. 18, p. 631–650, https://doi.org/10.1007/BF00313878.

Caress, D.W., and Chayes, D.N., 2017, MB-System: Mapping the Seafloor, https://www.mbari.org/products/research-software/mb-system.

Caress, D.W., Thomas, H., Kirkwood, W.J., McEwen, R., Henthorn, R., Clague, E.A., Paull, C.K., Paduan, J., and Maier, K.L., 2008, High-Resolution Multibeam, Sidescan, and Subbottom Surveys Using the MBARI AUV D. Allan B., *in* Reynolds, J.R., and Greene, H.G., eds., Marine Habitat Mapping Technology for Alaska: Alaska Sea Grant College Program, University of Alaska Fairbanks, https://doi.org/10.4027/mhmta.2008.04.

Carver, G., and Plafker, G., 2008, Paleoseismicity and Neotectonics of the Aleutian Subduction Zone—An Overview, *in* Freymueller, J.T., Haeussler, P.J., et al., eds., Active Tectonics and Seismic Potential of Alaska: American Geophysical Union: Geophysical Monograph 179, p. 1–42, https://doi.org/10.1029/179GM03.

Christensen, D.H., and Beck, S.L., 1994, The rupture process and tectonic implications of the great 1964 Prince William Sound earthquake: Pure and Applied Geophysics, v. 142, p. 29–53, https://doi.org/10.1007/BF00875967.

Christensen, D.H., and Ruff, L.J., 1983, Outer-rise earthquakes and seismic coupling: Geophysical Research Letters, v. 10, p. 697–700, https://doi.org/10.1029/GL010i008p00697.

Christensen, D.H., and Ruff, L.J., 1988, Seismic coupling and outer rise earthquakes: Journal of Geophysical Research, v. 93, p. 13,421–13,444, https://doi.org/10.1029/JB093iB11p13421.

Cohen, J.K., and Stockwell, J.W., Jr., 2017, CWP/SU: Seismic Un*x Release No. 44: An open source software package for seismic research and processing: Golden, Colorado, Center for Wave Phenomena, Colorado School of Mines.

Crutchley, G.J., Klaeschen, D., Henrys, S.A., Pecher, I.A., Mountjoy, J.J., and Woelz, S., 2020, Subducted sediments, upper-plate deformation and dewatering at New Zealand's southern Hikurangi subduction margin: Earth and Planetary Science Letters, v. 530, https://doi.org/10.1016/j.epsl.2019.115945.

Davis, D., Suppe, J., and Dahlen, F.A., 1983, Mechanics of fold-and-thrust belts and accretionary wedges: Journal of Geophysical Research, v. 88, p. 1153–1172, https://doi.org/10.1029/JB088iB02p01153.

Davis, D.M., and von Huene, R., 1987, Inferences on sediment strength and fault friction from structures at the Aleutian Trench: Geology, v. 15, p. 517–522, https://doi.org/10.1130/0091-7613(1987)15<517:IOSSAF>2.0.CO;2.

Delouis, B., Philip, H., Dorbath, L., and Cisternas, A., 1998, Recent crustal deformation in the Antofagasta region (northern Chile) and the subduction process: Geophysical Journal International, v. 132, p. 302–338, https://doi.org/10.1046/j.1365-246x.1998.00439.x.

DeMets, C., Gordon, R.G., and Argus, D.F., 2010, Geologically current plate motions: Geophysical Journal International, v. 181, no. 1, p. 1–80, https://doi.org/10.1111/j.1365-246X.2009.04491.x.

Dmowska, R., and Lovison, L.C., 1992, Influence of asperities along subduction interfaces on the stressing and seismicity of adjacent areas, *in* Mikumo, T., Aki, K., Ohnaka, M., Ruff, L.J., and Spudich, P.K.P., eds., Earthquake Source Physics and Earthquake Precursors: Tectonophysics 211, p. 23–43, https://doi.org/10.1016/0040-1951(92)90049-C.

Dominguez, S., Lallemand, S.E., Malavieille, J., and von Huene, R., 1998, Upper plate deformations associated with seamount subduction: Tectonophysics, v. 293, p. 207–224, no. 3–4, https://doi.org/10.1016/S0040-1951(98)00086-9.

Fan, W., Bassett, D., Jiang, J., Shearer, P.M., and Ji, C., 2017, Rupture evolution of the 2006 Java tsunami earthquake and the possible role of splay faults: Tectonophysics, v. 721, p. 143–150, https://doi.org/10.1016/j.tecto.2017.10.003.

Flueh, E.R., and Bialas, J., 1996, A digital, high data capacity ocean bottom recorder for seismic investigations: International Underwater System Design, v. 18, no. 3, p. 18–20.

Flueh, E.R., and von Huene, R., eds., 1994, FS Sonne Fahrtbericht SO96 Kodiak Seis, Hong Kong–Kodiak–Kodiak, 09.06.1994–26.07.1994: Geomar interner Fahrtbericht, GEOMAR Forschungszentrum für marine Geowissenschaften, Kiel, 214 p., https://doi.org10.3289/CR_SO_96.

Frederik, M.C., 2016, Morphology and structure of the accretionary prism offshore North Sumatra, Indonesia and offshore Kodiak Island, USA—A comparison to seek a link between prism formation and hazard potential [Ph.D. thesis]: Austin, Texas, University of Texas in Austin, 136 p.

Frederik, M.C.G., Gulick, S.P.S., and Miller, J.J., 2020, Effect on subduction of deeply buried seamounts offshore of Kodiak Island: Tectonics, v. 39, e2019TC005710, https://doi.org/10.1029/2019TC005710.

GEBCO Compilation Group, 2019, GEBCO 2019 Grid, https://doi.org/10.5285/836f016a-33be-6ddc-e053-6c86abc0788e.

Geersen, J., 2019, Sediment-starved trenches and rough subducting plates are conducive to tsunami earthquakes: Tectonophysics, v. 762, p. 28–44, https://doi.org/10.1016/j.tecto.2019.04.024.

Goes, S.D.B., 1996, Irregular recurrence of large earthquakes: An analysis of historic and paleoseismic catalogs: Journal of Geophysical Research, v. 101, p. 5739–5749, https://doi.org/10.1029/95JB03044.

Gulick, S.P.S., Lowe, L.A., Pavlis, T.L., Gardner, J.V., and Mayer, L.A., 2007, Geophysical insights into the Transition fault debate: Propagating strike slip in response to stalling Yakutat block subduction in the Gulf of Alaska: Geology, v. 35, no. 8, p. 763–766, https://doi.org/10.1130/G23585A.1.

Gulick, S.P.S., Jaeger, J.M., Mix, A.C., Asahi, H., Bahlburg, H., Belanger, C.L., Berbel, G.B.B., Cowan, E., Drab, L., Forwick, M., Fukumura, A., Ge, S., Gupta, S., Kioka, A., Konno, S., LeVay, L.J., Marz, C., Matsuzaki, K.M., McClymont, C.M., Muller, J., Nakamura, A., Ojima, T., Ribeiro, F.R., Ridgway, K.D., Romero, O.E., Slagle, A.L., Stoner, J.S., St-Onge, G., Suto, I., Walczak, M.D., Worthington, L.L., Bailey, I., Enkelmann, E., Reece, R., and Swartz, J.J., 2015, Mid-Pleistocene climate transition drives net mass loss from rapidly uplifting St. Elias Mountains, Alaska: Proceedings of the National Academy of Sciences of the United States of America, v. 112, no. 49, p. 15,042–15,047, https://doi.org/10.1073/pnas.1512549112.

Harders, R., Ranero, C.R., and Weinrebe, W., 2014, Characterization of submarine landslide complexes offshore Costa Rica: An evolutionary model related to seamount subduction, *in* Krastel, S., et al., eds., Submarine Mass Movements and Their Consequences: Switzerland, Springer International Publishers, Advances in Natural and Technological Hazards Research, v. 37, 34 p., https://doi.org/10.1007/978-3-319-00972-8_34.

Hubbert, M.K., and Rubey, W.W., 1959, Role of fluid pressure in mechanics of overthrust faulting: Geological Society of America Bulletin, v. 70, p. 115–166, https://doi.org/10.1130/0016-7606(1959)70[115:ROFPIM]2.0.CO;2.

Husen, S., Quintero, R., and Kissling, E., 2002, Tomographic evidence for a subducted seamount beneath the Gulf of Nicoya, Costa Rica: The cause of the 1990 Mw = 7.0 Gulf of Nicoya earthquake: Geophysical Research Letters, v. 29, no. 8, p. 79-1–79-4, https://doi.org/10.1029/2001GL014045.

Ichinose, G., Somerville, P., Thio, H.K., Graves, R., and O'Connell, D., 2007, Rupture process of the 1964 Prince William Sound, Alaska, earthquake from the combined inversion of seismic, tsunami, and geodetic data: Journal of Geophysical Research, v. 112, B07306, https://doi.org/10.1029/2006JB004728.

Johnson, J.M., and Satake, K., 1997, Estimation of seismic moment and slip distribution of the 1 April 1946, Aleutian tsunami earthquake: Journal of Geophysical Research, v. 102, p. 11,765–11,774, https://doi.org/10.1029/97JB00274.

Johnson, J.M., Satake, K., Holdahl, S.R., and Sauber, J., 1996, The 1964 Prince William Sound earthquake: Joint inversion of tsunami and geodetic data: Journal of Geophysical Research, v. 101, p. 523–532, https://doi.org/10.1029/95JB02806.

Kanamori, H., 1972, Mechanism of tsunami earthquakes: Physics of the Earth and Planetary Interiors, v. 6, p. 346–359, https://doi.org/10.1016/0031-9201(72)90058-1.

Kanamori, H., and Kikuchi, M., 1993, The 1992 Nicaragua earthquake: A slow tsunami earthquake associated with subducted sediments: Nature, v. 361, p. 714–716, https://doi.org/10.1038/361714a0.

Karig, D.E., 1990, Experimental and observational constraints on the mechanical behaviour in the toes of accretionary prisms, *in* Knipe, R.J., and Rutter, E.H., eds., Deformation Mechanisms, Rheology and Tectonics: Geological Society of London Special Publication 54, p. 383–398, https://doi.org/10.1144/GSL.SP.1990.054.01.35.

Kodaira, S., Takahashi, N., Nakanishi, A., Miura, S., and Kaneda, Y., 2000, Subducted seamount imaged in the rupture zone of the 1946 Nankaido earthquake: Science, v. 289, p. 104–106, https://doi.org/10.1126/science.289.5476.104.

Kopp, H., 2013, Invited review paper: The control of subduction zone structural complexity and geometry on margin segmentation and seismicity: Tectonophysics, v. 589, p. 1–16, https://doi.org/10.1016/j.tecto.2012.12.037.

Korenaga, J., and Sager, W.W., 2012, Seismic tomography of Shatsky Rise by adaptive importance sampling: Journal of Geophysical Research, v. 117, B08102, https://doi.org/10.1029/2012JB009248.

Korenaga, J., Holbrook, W.S., Kent, G.M., Keleman, P.B., Detrick, R.S., Larsen, H.-C., Hopper, J.R., and Dahl-Jensen, T., 2000, Crustal structure of the southeast Greenland margin from joint refraction and reflection seismic tomography: Journal of Geophysical Research, v. 105, p. 21,591–21,614, https://doi.org/10.1029/2000JB900188.

Krabbenhoeft, A., von Huene, R., Miller, J.J., Lange, D., and Vera, F., 2018, Strike-slip 23 January 2018 M7.9 Gulf of Alaska rare intraplate earthquake: Complex rupture of a fracture zone system: Nature Scientific Reports, v. 8, 13706, https://doi.org/10.1038/s41598-018-32071-4.

Lahr, J.C., Page, R.A., Stephens, C.D., and Christensen, D.H., 1988, Unusual earthquakes in the Gulf of Alaska and fragmentation of the Pacific plate: Geophysical Research Letters, v. 15, no. 13, p. 1483–1486, https://doi.org/10.1029/GL015i013p01483.

Lallemand, S., Schnürle, P., and Malavieille, J., 1994, Coulomb theory applied to accretionary and nonaccretionary wedges: Possible causes for tectonic erosion and/or frontal accretion: Journal of Geophysical Research, v. 99, p. 12,033–12,055, https://doi.org/10.1029/94JB00124.

Lallemand, S., Peyret, M., van Rijsingen, E., Arcay, D., and Heuret, A., 2018, Roughness characteristics of oceanic seafloor prior to subduction in relation to the seismogenic potential of subduction zones: Geochemistry, Geophysics, Geosystems, v. 19, p. 2121–2146, https://doi.org/10.1029/2018GC007434.

Lay, T., and Bilek, S., 2007, Anomalous Earthquake Ruptures at Shallow Depths on Subduction Zone Megathrusts, *in* Dixon, T.H., and Moore, C.J., eds., The Seismogenic Zone of Subduction Thrust Faults: New York, Columbia University Press, p. 476–511, https://doi.org/10.7312/dixo13866.

Lay, T., Ye, L., Bai, Y., Cheung, K.F., and Kanamori, H., 2018, The 2018 MW 7.9 Gulf of Alaska earthquake: Multiple fault rupture in the Pacific plate: Geophysical Research Letters, v. 45, p. 9542–9551, https://doi.org/10.1029/2018GL079813.

Lee, H.J., and von Huene, R., 1973, Physical properties of deformed sediments from site 181, *in* Kulm, L.D., von Huene R., et al., eds., 1973: Initial Reports of the Deep Sea Drilling Project, Volume 18: Washington, D.C., U.S. Government Printing Office, p. 897–902, https://doi.org/10.2973/dsdp.proc.18.127.1973.

Lim, E., Eakins, B.W., and Wigley, R., 2009, Southern Alaska coastal relief model: Procedures, data sources and analysis: Boulder, Colorado, National Oceanic and Atmospheric Administration, http://www.ngdc.noaa.gov/mgg/coastal/s_alaska.html.

Lizarralde, D., Holbrook, W.S., McGeary, S., Bangs, N.L., and Diebold, J.B., 2002, Crustal construction of a volcanic arc; wide-angle seismic results from the western Alaska Peninsula: Journal of Geophysical Research, v. 107, 2164, https://doi.org/10.1029/2001JB000230.

Lotto, G.C., Jeppson, T.N., and Dunham, E.M., 2019, Fully Coupled Simulations of Megathrust Earthquakes and Tsunamis in the Japan Trench, Nankai Trough, and Cascadia Subduction Zone: Pure and Applied Geophysics, v. 176, p. 4009–4041, https://doi.org/10.1007/s00024-018-1990-y.

Loveless, J.P., Hoke, G.D., Allmendinger, R.W., González, G., Isacks, B.L., and Carrizo, D.A., 2005, Pervasive cracking of the northern Chilean Coastal Cordillera: New evidence for forearc extension: Geology, v. 33, no. 12, p. 973–976, https://doi.org/10.1130/G22004.1.

Loveless, J.P., Allmendinger, R.W., Pritchard, M.E., and González, G., 2010, Normal and reverse faulting driven by subduction zone cycle in the northern Chilean fore arc: Tectonics, v. 29, https://doi.org/10.1029/2009TC002465.

Martínez-Loriente, S., Sallarès, V., Ranero, C.R., Ruh, J.B., Barckhausen, U., Grevemeyer, I., and Bangs, N., 2019, Influence of incoming plate relief on overriding plate deformation and earthquake nucleation: Cocos Ridge subduction (Costa Rica): Tectonics, v. 38, p. 4360–4377, https://doi.org/10.1029/2019TC005586.

Miller, J.J., and von Huene, R., 1987, Migrated seismic reflection lines, Eastern Aleutian Trench: U.S. Geological Survey Oil and Gas Investigations Chart OC-129.

Mochizuki, K., Yamada, T., Shinohara, M., and Yamanaka, Y., 2008, Weak Interplate Coupling by Seamounts and Repeating M ~ 7 Earthquakes: Science, v. 321, p. 1194–1197, https://doi.org/10.1126/science.1160250.

Moore, G.F., Bangs, N.L., Taira, A., Kuramoto, S., Pangborn, E., and Tobin, H.J., 2007, Three-dimensional splay fault geometry and implications for tsunami generation: Science, v. 318, p. 1128–1131, https://doi.org/10.1126/science.1147195.

Moser, T.J., 1991, Shortest path calculation of seismic rays: Geophysics, v. 56, p. 59–67, https://doi.org/10.1190/1.1442958.

Moser, T.J., Nolet, G., and Snieder, R., 1992, Ray bending revisited: Bulletin of the Seismological Society of America, v. 82, p. 259–288.

Naugler, F.P., and Wageman, J.M., 1973, Gulf of Alaska: Magnetic Anomalies, Fracture Zones, and Plate Interaction: Bulletin of the Geological Society of America, v. 84, no. 5, p. 1575–1584, https://doi.org/10.1130/0016-7606(1973)84<1575:GOAMAF>2.0.CO;2.

Plafker, G., 1965, Tectonic deformation associated with the 1964 Alaskan earthquake: Science, v. 148, p. 1675–1687, https://doi.org/10.1126/science.148.3678.1675.

Plafker, G., 1987, Application of marine-terrace data to paleoseismic studies, *in* Crone, A.J., and Omdahl, E.M., eds., Proceedings of Conference XXXIX—Directions in Paleoseismology: U.S. Geological Survey Open-File Report 87-92, p. 146–156.

Plafker, G., Lajoie, K.R., and Rubin, M., 1992, Determining Recurrence Intervals of Great Subduction Zone Earthquakes in Southern Alaska by Radiocarbon Dating, *in* Taylor, R.E., Long, A., and Kra, R.S., eds., Radiocarbon After Four Decades: New York, Springer, p. 436–453, https://doi.org/10.1007/978-1-4757-4249-7_28.

Ranero, C.R., Grevemeyer, I., Sahling, H., Barckhausen, U., Hensen, C., Wallmann, K., Weinrebe, W., Vannucchi, P., von Huene, R., and McIntosh, K., 2008, Hydrogeological system of erosional convergent margins and its influence on tectonics and interplate seismogenesis: Geochemistry, Geophysics, Geosystems, v. 9, Q03S04, https://doi.org/10.1029/2007GC001679.

Reece, R.S., Gulick, S.P.S., Horton, B.K., Christeson, G.L., and Worthington, L.L., 2011, Tectonic and climatic influence on the evolution of the Surveyor Fan and Channel system, Gulf

of Alaska: Geosphere, v. 7, p. 830–844, https://doi.org/10.1130/GES00654.1.
Reece, R.S., Gulick, S.P.S., Christeson, G.L., Horton, B.K., van Avendonk, H., and Barth, G., 2013, The role of farfield tectonic stress in oceanic intraplate deformation: Gulf of Alaska: Journal of Geophysical Research, Solid Earth, v. 118, p. 1862–1872, https://doi.org/10.1002/jgrb.50177.
Reimnitz, E., 1966, Late Quaternary history and sedimentation of the Copper River Delta and vicinity, Alaska [Ph.D. thesis]: University of California, San Diego, 160 p.
Robinson, D.P., Das, S., and Watts, A.B., 2006, Earthquake rupture stalled by a subducting fracture zone: Science, v. 312, p. 1203–1205.
Rosenbaum, G., and Mo, W., 2011, Tectonic and magmatic responses to the subduction of high bathymetric relief: Gondwana Research, v. 19, no. 3, p. 571–582, https://doi.org/10.1016/j.gr.2010.10.007.
Ruff, L.J., 1989, Do trench sediments affect great earthquake occurrence in subduction zones?: Pure and Applied Geophysics, v. 129, p. 263–282, https://doi.org/10.1007/BF00874629.
Ruppert, N.A., Rollins, C., Zhang, A., Meng, L., Holtkamp, S.G., West, M.E., and Freymueller, J.T., 2018, Complex faulting and triggered rupture during the 2018 MW 7.9 offshore Kodiak, Alaska, earthquake: Geophysical Research Letters, v. 45, p. 7533–7541, https://doi.org/10.1029/2018GL078931.
Saffer, D.M., and Tobin, H.J., 2011, Hydrogeology and Mechanics of Subduction Zone Forearcs: Fluid Flow and Pore Pressure: Annual Review of Earth and Planetary Sciences, v. 39, no. 1, p. 157–186, https://doi.org/10.1146/annurev-earth-040610-133408.
Sahling, H., Masson, D.G., Ranero, C.R., Hühnerbach, V., Weinrebe, W., Klaucke, I., Bürk, D., Brückmann, W., and Suess, E., 2008, Fluid seepage at the continental margin offshore Costa Rica and southern Nicaragua: Geochemistry, Geophysics, Geosystems, v. 9, Q05S05, https://doi.org/10.1029/2008GC001978.
Sallarès, V., and Ranero, C.R., 2005, Structure and tectonics of the erosional convergent margin off Antofagasta, north Chile (23°30′S): Journal of Geophysical Research, v. 110, p. B06101, https://doi.org/10.1029/2004JB003418.
Sallarès, V., and Ranero, C.R., 2019, Upper-plate rigidity determines depth-varying rupture behaviour of megathrust earthquakes: Nature, v. 576, p. 96–101, https://doi.org/10.1038/s41586-019-1784-0.
Sandwell, D.T., Müller, R.D., Smith, W.H.F., Garcia, E., and Francis, R., 2014, New global marine gravity model from CryoSat-2 and Jason-1 reveals buried tectonic structure: Science, v. 346, no. 6205, p. 65–67, https://doi.org/10.1126/science.1258213.
Sauber, J., Carver, G., Cohen, S., and King, R., 2006, Crustal deformation and the seismic cycle across the Kodiak Islands, Alaska: Journal of Geophysical Research, v. 111, B02403, https://doi.org/10.1029/2005JB003626.
Savage, J.C., Svarc, J.L., and Prescott, W.H., 1999, Deformation across the Alaska-Aleutian Subduction Zone near Kodiak: Geophysical Research Letters, v. 26, p. 2117–2120, https://doi.org/10.1029/1999GL900471.
Scholl, D.W., Kirby, S.H., von Huene, R., Ryan, H., Wells, R.E., and Geist, E.L., 2015, Great (≥Mw8.0) megathrust earthquakes and the subduction of excess sediment and bathymetrically smooth seafloor: Geosphere, v. 11, no. 2, p. 236–265, https://doi.org/10.1130/GES01079.1.
Scholz, C.H., and Small, C., 1997, The effect of seamount subduction on seismic coupling: Geology, v. 25, p. 487–490, https://doi.org/10.1130/0091-7613(1997)025<0487:TEOSSO>2.3.CO;2.
Shillington, D.J., Becel, A., Nedimovic, M.R., Webb, S.C., Kuehn, H., Abers, G.A., et al., 2015, Link between plate fabric, hydration and subduction zone seismicity in Alaska: Nature Geoscience, v. 8, p. 961–964, https://doi.org/10.1038/ngeo2586.
Sladen, A., and Trevisan, J., 2018, Shallow megathrust earthquake ruptures betrayed by their outer-trench aftershocks signature: Earth and Planetary Science Letters, v. 483, p. 105–113, https://doi.org/10.1016/j.epsl.2017.12.006.
Stevenson, A.J., and Embley, R., 1987, Deep-sea fan bodies, terrigenous turbidite sedimentation, and petroleum geology, Gulf of Alaska: Geology and resources off western North America: Circum-Pacific Council for Energy and Mineral Resources: Earth Science Series, v. 6, p. 503–522.
Suess, E., 1994, FS Sonne Fahrtbericht SO97 Kodiak Vent, Kodiak–Dutch Harbour–Tokio–Singapur, 27.07.–19.09.1994: GEOMAR-Report 29, GEOMAR Forschungszentrum für marine Geowissenschaften, Kiel, https://doi.org/10.3289/GEOMAR_REP_29_1994.
Suess, E., Bohrmann, G., von Huene, R., Linke, P., Wallmann, K., Lammers, S., Sahling, H., Winckler, G., Lutz, R.A., and Orange, D., 1998, Fluid venting in the eastern Aleutian Subduction Zone: Journal of Geophysical Research, v. 103, p. 2597–2614, https://doi.org/10.1029/97JB02131.
Suito, H., and Freymueller, J.T., 2009, A viscoelastic and afterslip postseismic deformation model for the 1964 Alaska earthquake: Journal of Geophysical Research, v. 114, https://doi.org/10.1029/2008JB005954.
Sun, T., Saffer, D., and Ellis, S., 2020, Mechanical and hydrological effects of seamount subduction on megathrust stress and slip: Nature Geoscience, v. 13, p. 249–255, https://doi.org/10.1038/s41561-020-0542-0.
Tobin, H., and Saffer, D.M., 2009, Elevated fluid pressure and extreme mechanical weakness of a plate boundary thrust, Nankai Trough subduction zone: Geology, v. 37, p. 679–682, https://doi.org/10.1130/G25752A.1.
Todd, E.K., Schwartz, S.Y., Mochizuki, K., Wallace, L.M., Sheehan, A.F., Webb, S.C., Williams, C.A., Nakai, J., Yarce, J., Fry, B., Henrys, S., and Ito, Y., 2018, Earthquakes and tremor linked to seamount subduction during shallow slow slip at the Hikurangi Margin, New Zealand: Journal of Geophysical Research. Solid Earth, v. 123, p. 6769–6783, https://doi.org/10.1029/2018JB016136.
Toomey, D.R., and Foulger, G.R., 1989, Tomographic inversion of local earthquake data from the Hengill-Grensdalur central volcano complex, Iceland: Journal of Geophysical Research, v. 94, p. 17,497–17,510, https://doi.org/10.1029/JB094iB12p17497.
Turner, R.F., Lynch, M.B., Conner, T.A., Halin, P.J., Hoose, P.I., Martin, G.C., Olson, D.L., Larson, J.A., Fett, T.O., Sherwood, K.W., and Adams, A.J., 1987, Geological and operational summary, Kodiak Shelf stratigraphic test wells, western Gulf of Alaska: U.S. Department of the Interior Minerals Management Service OCS Report MMS 87–0109, 341.
U.S. Geological Survey, 2011, GAK_Q40.tif – Gulf of Alaska U.S. EEZ GLORIA sidescan-sonar data mosaic (10 of 30) (LCC, 50 m, WGS84): Menlo Park, California, U.S. Geological Survey Open-File Report 2010-1332, Coastal and Marine Geology Program, Pacific Coastal and Marine Science Center, downloaded November 2019 at https://pubs.usgs.gov/of/2010/1332/gloria_data/gulf_of_alaska/gak_q40.zip.
von Huene, R., Klaeschen, D., Gutscher, M., and Frühn, J., 1998, Mass and fluid flux during accretion at the Alaska margin: Geological Society of America Bulletin, v. 110, p. 468–482, https://doi.org/10.1130/0016-7606(1998)110<0468:MAFFDA>2.3.CO;2.
von Huene, R., Ranero, C.R., and Scholl, D., 2009, Convergent margin structure in high-quality geophysical images and current kinematic and dynamic models, *in* Lallemand, S., and Funiciello, F., eds., Subduction Zone Geodynamics: Berlin, Heidelberg, Springer, p. 137–157, https://doi.org/10.1007/978-3-540-87974-9_8.
von Huene, R., Miller, J., and Weinrebe, W., 2012, Subducting plate geology in three great earthquake ruptures on the western Alaska margin, Kodiak to Unimak: Geosphere, v. 8, https://doi.org/10.1130/GES00715.1.
von Huene, R., Miller, J.J., and Dartnell, P., 2015, A possible transoceanic tsunami directed toward the U.S. west coast from the Semidi segment, Alaska convergent margin: Geochemistry Geophysics Geosystems, v. 17, p. 645–659, https://doi.org/10.1002/2015GC006147.
von Huene, R., Miller, J.J., Klaeschen, D., and Dartnell, P., 2016, A Possible Source Mechanism of the 1946 Unimak Alaska Far-Field Tsunami: Uplift of the Mid-Slope Terrace Above a Splay Fault Zone: Pure and Applied Geophysics, v. 2016, https://doi.org/10.1007/s00024-016-1393-x.
von Huene, R., Miller, J.J., and Krabbenhoeft, A., 2019, The Shumagin seismic gap structure and associated tsunami hazards, Alaska convergent margin: Geosphere, v. 15, p. 324–341, https://doi.org/10.1130/GES01657.1.
von Huene, R., Miller, J.J., and Krabbenhoeft, A., 2020, The Alaska convergent margin backstop splay fault zone, a potential large tsunami generator between the frontal prism and continental framework: Geochemistry Geophysics Geosystems, https://doi.org/10.1029/2019GC008901.
Wang, K., and Bilek, S.L., 2011, Do subducting seamounts generate or stop large earthquakes?: Geology, v. 39, no. 9, p. 819–822, https://doi.org/10.1130/G31856.1.
Wang, K., and Bilek, S.L., 2014, Fault creep caused by subduction of rough seafloor relief: Tectonophysics, v. 610, p. 1–24, https://doi.org/10.1016/j.tecto.2013.11.024.
Watts, A.B., Koppers, A.P., and Robinson, D.P., 2010, Seamount Subduction and Earthquakes: Oceanography, v. 23, no. 1, p. 166–173, https://doi.org/10.5670/oceanog.2010.68.
Weatherall, P., Marks, K.M., Jakobsson, M., Schmitt, T., Tani, S., Arndt, J.E., Rovere, M., Chayes, D., Ferrini, V., and Wigley, R., 2015, A new digital bathymetric model of the world's oceans: Earth and Space Science, v. 2, p. 331–345, https://doi.org/10.1002/2015EA000107.
Wendt, J., Oglesby, D.D., and Geist, E.L., 2009, Tsunamis and splay fault dynamics: Geophysical Research Letters, v. 36, L15303, https://doi.org/10.1029/2009GL038295.
Wessel, P., and Smith, W.H.F., 1998, New, improved version of the Generic Mapping Tools released: Eos, v. 79, p. 579, https://doi.org/10.1029/98EO00426.
Winston, J.G., 1983, Kodiak Shelf, Gulf of Alaska: Tulsa, Oklahoma, American Association of Petroleum Geology, Studies in Geology, v. 15, no. 3, p. 140–146.